Quantum Reflection in Two Dimensions

Emanuele Galiffi

Department of Physics

Imperial College London - University of Heidelberg

This dissertation is submitted for the degree of

MSci Physics

To my family: Francesco, Mariangela and Davide.

Declaration

This project is embedded in a larger project with a long-term perspective in the numerical study of quantum reflection (QR) in atom-surface scattering problems. The project leaders are Sandro Wimberger (University of Parma, University of Heidelberg) and Dr. Maarten DeKieviet (University of Heidelberg). The first project, which was carried out by B. Herwerth, concerned the development and implementation of numerical time-dependent methods used in 1D studies. These found an application in the study of QR off vibrating surfaces. In the second project, which was carried out by Sünderhauf, different approaches to 2D wavepacket propagation were considered from a general point of view. The computational costs associated to the matrix decomposition of the 2D Hamiltonian matrix were estimated in that context. Furthermore, comparisons were drawn between quantum and classical reflection, and methods for isolating the two effects were investigated. Moreover, part of the 1D *Fortran* code written by Herwerth was translated by Sünderhauf in *C++*.

I hereby declare that except where specific reference is made to the work of others, the contents of this dissertation are original and have not been submitted in whole or in part for consideration for any other degree or qualification in this, or any other university. This dissertation is my own work and contains nothing which is the outcome of work done in collaboration with others, except as specified in the text and Acknowledgements.

In the present project, preliminary studies were performed on 1D systems by means of the code written by Sünderhauf. The interpretation of these results was crucial in order to understand the response of our numerical method to the characteristic parameters of typical QR problems. The major efforts in this project involved the implementation of the numerical routines which will enable complete 2D studies of QR to be performed. The Cholesky decomposition attempted by Sünderhauf was completed. Different propagation algorithms were investigated and the most efficient was chosen and implemented.

Propagation tests were performed on known 2D systems and compared in real space to analytic solutions. As soon as such tests were qualitatively successful, 1D results for QR at a flat attractive surface were reproduced by means of our 2D code on a separable potential of the same type. Such result represents the major success of this project.

Furthermore, preliminary tasks towards the implementation of an appropriate potential for a study of QR off 2D corrugated surfaces were undertaken.

Emanuele Galiffi

July 2015

Acknowledgements

Abstract

The numerical propagation of a wavepacket in two dimensions (2D) finds a wide range of applications in scattering problems. In this project, a highly optimised, norm-preserving algorithm is implemented and tested, in order to numerically solve the Time-Dependent Schrödinger Equation in 2D. The aim of our study is to provide a proof of concept that quantum reflection (QR) from 2D periodic potential structures can be studied using our numerical method. To this end, the numerical procedures used are presented, as well as the propagation tests performed with them. The key objective achieved is the match with 1D results for QR at a flat surface. Finally, an effective 2D potential for a corrugated surface is proposed for the short-range regime. Future tests of QR on such potential will enable the first comparisons with experimental results for QR off corrugated surfaces. This enables the systematic investigation of atom-surface potentials where Casimir interactions are relevant, as well as numerical tests on quantum diffraction.

Zusammenfassung

Die numerische Berechnung der Ausbreitung eines Wellenpakets in zwei Dimensionen (2D) findet breite Anwendung in Streuproblemen. In dieser Arbeit wird ein hochgradig optimierter, normierungserhaltender Algorithmus implementiert und getestet, um die Zeitabhängige Schrödingergleichung zu lösen, die die Propagation eines Wellenpakets in 2D in der Zeit beschreibt. Das Ziel dieser Arbeit ist ein "proof of concept", dass mit unseren numerischen Methoden die Quantenreflexion (QR) an zweidimensionalen periodischen Potenzialen studiert werden kann. Dazu werden die numerischen Verfahren, sowie die Ausbreitungstests präsentiert. Das Hauptergebnis ist die Übereinstimmung der Ergebnisse von QR an einer flachen Oberfläche mit dem Ergebnis des eindimensionalen Problems. Schliesslich wird ein effektives zweidimensionales Potenzial für den Nahfeldbereich einer geriffelten Oberfläche vorgeschlagen. Zukünftige Berechnungen der Quantenreflexion an einem solchen Potenzial werden die ersten Vergleiche mit experimentellen Resultaten der QR an geriffelten Oberflächen erlauben. Dies ermöglicht die systematische Untersuchung von Atom-Oberflächen-Potenzialen, in denen Casimir-Wechselwirkungen relevant sind, sowie numerische Tests der quantenmechanischer Streuung.

Table of contents

Chapter 1

Introduction

Over the last decade, experimental advances in the techniques for cooling and control of atoms [47] stimulated a strong scientific interest in a variety of problems related to the scattering of slow neutral particles as they interact with surfaces. In the ultracold (10^{-3} m $s^{-1} < v < 10^{-2}$ m s^{-1}) regime, remarkable advances were made by Shimizu et al. [47], who managed to study experimentally quantum reflection (QR) of metastable Neon atoms, that scatter at normal incidence from Silicon and BK7 glass surfaces. At higher energy scales ($v \sim 1$ m s^{-1}), scattering at grazing incidence has enabled the systematic investigation of QR by the use of well-collimated atomic beams.

QR has recently attracted an increasing interest as a consequence of the achievement of energy measurements at unprecedented levels of precision. The Atomic Beam Spin Echo apparatus in Heidelberg can be used to measure the energy of atoms at the neV scale [13–15, 34]. In contrast to most other atom-interferometers, the ABSE technique uses a ground state noble gas atom (^{3}He) as a probe particle. This guarantees that the interaction with the surface is chemically inert, which makes ABSE unique with respect to all other slow atom control techniques [16]. Since QR is extremely sensitive to atom-surface interactions far out in the sub-μeV regime, this effect can be used as an ideal tool for tests of the theories which investigate retardation in these interactions.

Their study is important for a wide range of areas of physics, which range from quantum field theory to technological applications, as described below.

In atomic physics, QR may become in the near future an effective tool for atom guiding [19]. In fact, whereas the manipulation of atoms by means of lasers is highly sensitive to the wavelength of the laser used, the dependence of QR on the wavelength of the particle is

much less restrictive, so that groups of different atoms could be controlled without need for individual laser frequencies[1] [12].

Furthermore, QR finds important applications in neutron physics, since it plays a key role in the design of supermirrors for neutron production [35]. In fact, neutrons are scattered off surfaces as a result of the strong interaction with the nuclei in the material [36]. This effect is generally described by the Fermi pseudo-potential [5, 48]. Beside the well-established use in nuclear reactors, neutrons find applications in a wide range of scattering problems. In fact, they can be slowed down to very low velocities (in the $meV - neV$ energy regime) [35]. Thus, they can replace X-Rays in the study of biomolecular structures and phonon dynamics in solids, when the typical energy scales of the system studied are too low to be resolved accurately via X-Ray scattering, whose energy range is of the order of keV. In addition, the study of neutron scattering allows time of flight, as well as spin echo measurements to be performed, in contrast to X-Rays [35], to study inelastic scattering.

Finally, the high sensitivity of QR to the potential landscape allows effective surface potentials to be investigated by matching the reflectivity of theoretically predicted potentials to the experimental values observed. Clearly, this application has a fundamental importance in all other fields mentioned.

The central aim of this project is to develop the computational machinery which will enable the study of QR in two dimensions from several potential structures. In particular, as will be shown later, the 2D method developed lends itself to the study of QR off 2D periodic potentials.

To this end, a number of objectives were formulated:

1. The problem of quantum reflection was reviewed and studied in 1D in the context of known potential structures, in order to achieve an understanding of the behaviour of the reflection coefficient. The currently available methods in the study of QR were reviewed.

2. The computational methods for the propagation of wavepackets in time were developed and the algorithms were written using an Object-Oriented Programming (OOP) approach.

3. The code developed was tested by propagating wavepackets across a number of potential structures, whose exact analytical solution or qualitative dynamics can be predicted. The convergence and stability of the results was tested for the different potentials used.

---

[1]This is due to the fact that frequencies which are far from atomic resonances also contribute significantly to fluctuation forces (see Sec.1.1).

4. The results for QR from atom-surface potentials of the Casimir-Van der Waals $1/x^3$ type [22], previously obtained in 1D by Herwerth et al.[29], were then successfully reproduced with the new 2D code.

5. The method used in previous 1D studies for treating QR from atom-surface potentials were generalised to 2D.

6. Finally, starting from the Van der Waals attractive potential for a flat surface, a generalisation of such potential is computed for corrugated surfaces. Future tests on this potential will be the first results for QR of truly 2D surfaces.

Our simulations will then model experiments which can be performed using the Atom Beam Spin Echo (ABSE) technique in Heidelberg for the measurement of QR of slow ^{3}He atoms approaching a periodically, uniaxially corrugated gold surface.

This report is structured as follows: in the present chapter an overview of the key aspects of this project and its previous stages is given. Moreover, the results obtained at its previous stages are briefly described as they form a necessary background to the present work. The numerical methods implemented for the propagation of wavepackets in 2D are described in detail in Chapter two, whereas the results of numerical tests performed with them are presented in the third Chapter. Finally, in Chapter four the first steps towards the implementation of a full study of QR off true 2D surfaces are described.

1.1   Casimir interactions

In 1948 the Dutch Physicist Hendrik Casimir predicted [9] the existence of an attractive force between two plates due to vacuum fluctuations. The idea behind it was the following: the zero-point energy of a quantised electric field is not zero. As a consequence, the vacuum contains energy in the form of photon pairs which are continuously created and annihilated. However, when two uncharged metallic plates are placed next to each others, their presence imposes, as a consequence of Maxwell's equations, boundary conditions on the spectrum of the vacuum fluctuations. More specifically, their wavefunctions must be zero at the surface of the plates. This constraint restricts the number of allowed modes of such photons between the two plates, so that an energy gradient arises between the outer vacuum regions and the region between the plates. Such energy gradient, which is a consequence of the unbalanced allowed number of photons in the different regions, results in an attractive force between the plates.

One year later, Casimir, together with Polder, extended this idea to the case of a neutral atom approaching a metallic plate. In fact, a similar effect arises as a consequence of the
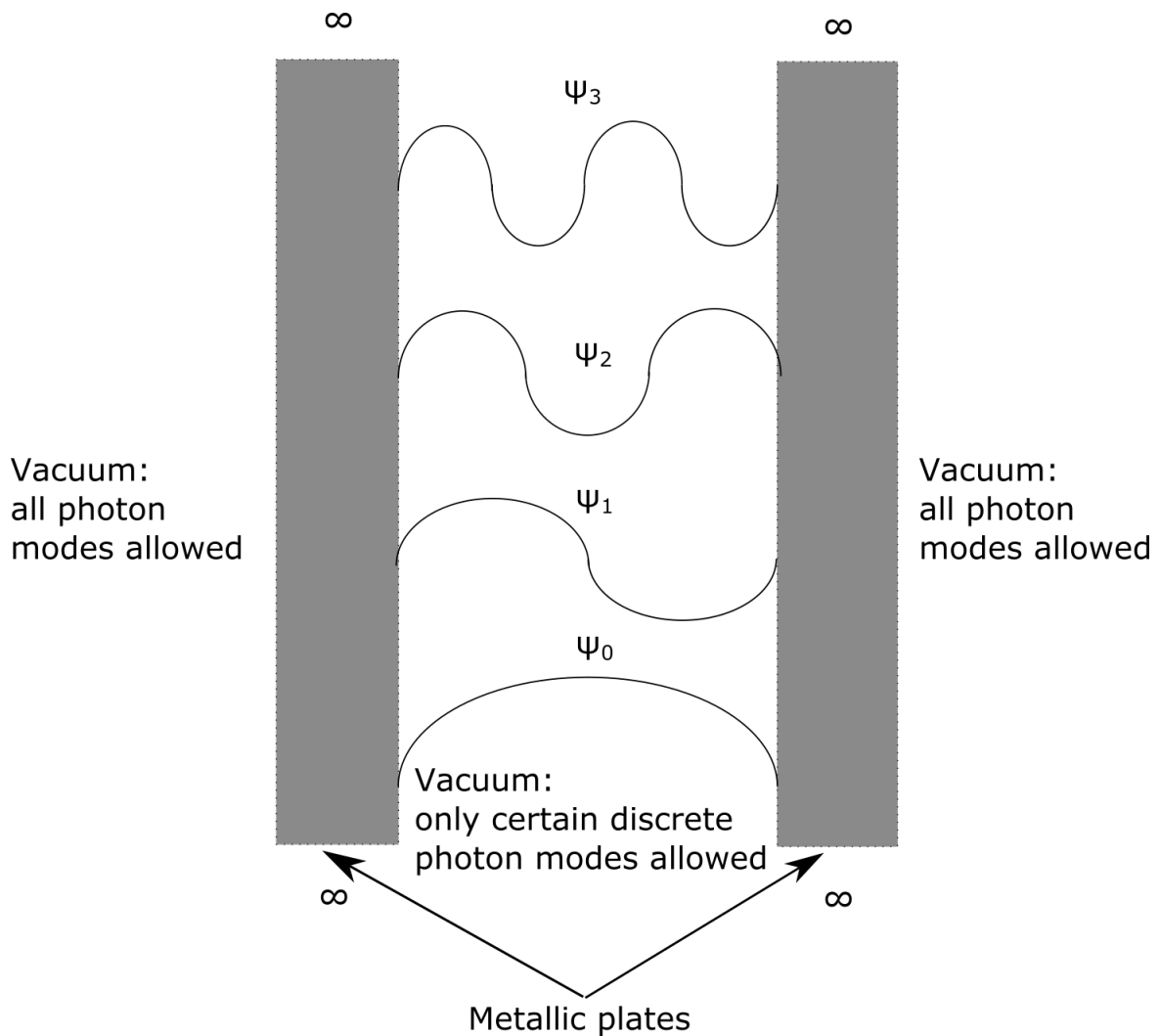
Fig. 1.1 The diagram shows the setup for which Casimir calculated the attractive force between two infinite plates. While in the outer regions all fluctuation modes are allowed, the region between the two plates can only host a discrete set of modes which satisfy the boundary conditions. As a result, a net attractive force between the two plates arises.

possibility of an electric dipole transition to occur in the atom. The Casimir-Polder potential for the interaction of an atom with a flat surface can be conveniently approximated as [37, 42]:

$$V(x) = -\frac{C_4}{x^3(x+\lambda)} \tag{1.1}$$

where x is the normal distance between the atom and the surface, C_4 is a strength constant which depends on the properties of the atom and the surface material, and λ is the reduced

wavelength of the electric dipole transition, which only depends on the atom in question [38]. In the case of ^{3}He, $\lambda \approx 9.3nm$.

The Casimir effect has been shown to be intimately related to Van der Waals forces, which arise as a consequence of the interaction between electric dipoles [2]. This can be seen from from Eq.(1.1), which recovers the well-known $1/x^3$ behaviour for the Van der Waals interaction between an atom and a wall for $x \ll \lambda$ In fact, the Casimir effect has been described as a relativistic generalisation of the Van der Waals force [32].

Compared to the Van der Waals force, which generally behave as x^{-3}, the Casimir-Polder potential includes an extra factor of $(x+\lambda)^{-1}$, which accounts for retardation effects. The effect of retardation, for $x \geq \lambda$ is to weaken the Van der Waals interaction, as a result of the phase difference between the charge fluctuations which are responsible for the interaction.

In addition to this attractive force, an effective repulsion becomes relevant as the electronic cloud of the atom and the surfaces become too close. Such repulsion is a consequence of Pauli principle [3], and its strength decays exponentially with the distance to the surface, so that the complete interaction is described by:

$$V(x) = Ae^{-Kx} - \frac{C_4}{x^3(x+\lambda)} \tag{1.2}$$

where A, K, λ and C_3 are characteristic for the materials involved [31, 50, 52].

In this work, only the attractive regime is considered. The effect of repulsive interaction, which is responsible for classical reflection, was investigated by Sünderhauf [50]. In the short-range attractive regime, where $x \ll \lambda$, retardation effects become negligible, so that the effective potential for a flat surface is given by the Casimir-Van der Waals potential

$$V(x) \simeq -\frac{C_3}{x^3} \tag{1.3}$$

where $C_3 = \frac{C_4}{\lambda}$.

For simplicity, this form of the atom-surface potential was used in all simulations which our codes were tested on.

In general, calculations of Casimir-Polder forces for arbitrary surface geometries are highly non-trivial. Nevertheless, the interaction potential has been calculated for a number of different geometries [11, 41]. This work focuses on the potential which results from the interaction of a neutral atom with a periodically corrugated surface. To the best knowledge of the author, no analytical form has been calculated for this surface geometry so far. Nevertheless, a numerical study was performed in [17]. The computational machinery developed in this

---

[2]In the case of atom-surface interactions a mirror dipole is formed in the surface as a result of dipole fluctuations.

project will later be used to perform tests of such numerical potential in order to compare the results with experimental data available in Heidelberg.

An estimate of this potential is proposed (see Sec. 4.1) for the non-retarded regime, where the contributions from individual interactions in the solid may be assumed to be additive, as described by the so-called Hamaker approximation.

Finally, Casimir interactions need not be attractive. In fact, the existence of repulsive Casimir forces has been proved for certain geometries [40]. A deeper knowledge of such forces is thus expected to lead to remarkable advances in the field of quantum tribology [4, 8, 46]. [3] For more details on the Casimir effect I hereby refer to [2].

1.2   Quantum reflection

In classical physics, energy restrictions impose strict limits on the spatial regions which a particle is allowed to occupy. Namely, a classical point-particle with total energy $E > 0$, which approaches a region of potential energy V will:

- Enter such region (transmission) if its energy $E > V$.

- Be reflected back if its energy $E < V$.

However, in the quantum domain these restrictions are not so sharp anymore. The most well-known case is the tunneling of a particle through a potential barrier $V(x) > E$. In this case a quantum particle would be able to reach a region which is classically forbidden with a finite probability. However, the opposite effect can also occur. Namely, a particle with $E > V(x)$, which would classically enter the new region, can be reflected as a result of a sudden change in the potential. In the rest of this thesis, we will refer to this effect as QR, although the scattering mechanism can be understood from fundamental quantum mechanics [24]. The most astounding aspect of this effect is the fact that it does not depend on the sign of the change in the potential. Thus, a decrease in the potential energy would result in an equivalent reflection coefficient as a potential increase of the same extent. In a classical picture, the former case would correspond to a particle, whose change in momentum opposes the force applied to it, which is evidently in contradiction with Newton's second Law.

Hence, as opposed to classical reflection (CR), which occurs when $E < V$ and finds a direct analogue in classical physics, QR has no classical analogue in classical particle

---

[3]The term "tribology" denotes the equivalent of friction in the quantum regime.

mechanics, which means that it can only be observed in the quantum regime. In fact, the occurrence of QR is intimately related to the wave nature of quantum particles[4].

It is necessary to determine the regime at which the wave nature of quantum particles becomes significant. To this end, a standard approach is to consider the conditions under which the semiclassical Wenzel-Kramers-Brillouin (WKB) approximation fails in describing the dynamics of the particle [21] [18].

The accuracy of the WKB approximation is governed by the badlands function [26]:

$$|B(X)| = \hbar^2 \left| \frac{3}{4} \frac{(p\prime)^2}{p^4} - \frac{1}{2} \frac{p\prime\prime}{p^3} \right| \ll 1 \qquad (1.4)$$

where $p(x)$ is the local momentum and $p\prime$ and $p\prime\prime$ are its first and second spatial derivatives respectively.

By assuming that the second derivative of the momentum of the particle is negligible compared to its value, a slightly less stringent, but more insightful condition can be derived from Eq.(1.4):

$$\frac{\left| \frac{dV}{dx} \right|}{|E - V(x)|} \lambda_{DB} \ll 1 \qquad (1.5)$$

where $V(x)$ is the local value of the potential energy, E is the total energy of the particle, and λ_{DB} is the De Broglie wavelength [22].

Eq.(1.5) shows clearly that the condition for the WKB approximation to hold is that the change in the slope of the potential within the spatial extent of a De Broglie wavelength must be negligible compared to its kinetic energy. Hence, given a certain slope of the potential, QR is expected to occur in the range where the energy of the incoming particle is comparable to the absolute value of the potential [53].

Hence, the occurrence of QR characterises the transition from a semiclassical regime to a purely quantum regime, where the wave nature of matter becomes important.

However, this treatment is only valid in 1D. In the case of 2D non-separable scattering potentials, the prediction of the position where QR would occur becomes highly non-trivial. A comprehensive theoretical account of QR theory can be found in [18], while the present work focuses on the time-dependent numerical treatment of QR problems in 2D, which, to the best knowledge of the author, has never been achieved before.

---

[4]Technically, reflection is described as a result of a phase mismatch at positions where the existence of bound states imposes conditions on the amplitude of the wave.

1.3   Numerical wavepacket propagation

So far, numerical studies of QR problems have been performed mainly by means of time-independent approaches. Typically, such methods allow one to determine the reflection coefficient by assuming a certain wave form for the solutions at the boundaries of the numerical box, and solving the time-independent Schrödinger Equation (TISE) for a given (time-independent) potential. Such a procedure has a number of advantages compared to a time-dependent treatment. In fact the solution of the TISE is a computationally simpler and less expensive task compared to a full time-dependent calculation, which involves the solution of a partial differential equation. Therefore, this approach is a standard choice in quantum scattering problems in the case of stationary potentials. An application of this method to our initial 1D problem is briefly presented below, while more comprehensive treatments can be found in [7, 26].

However, since for a 2D non-separable potential the wavefunction cannot in general be factorised, this method cannot be applied to the case of a 2D non-separable potential [54]. Therefore, a time-dependent approach is used in this work.

1.3.1   Time-dependent numerical approach

As opposed to stationary approaches, time-dependent methods leave a wider range of possibilities, including time-varying potentials and the propagation of wavepacket across non-separable 2D potentials. Clearly the computational costs of such tasks is far higher than in the time-independent case. The techniques which were used in this work are well established methods in numerical analysis, and have been applied to quantum mechanical problems in a variety of cases [23, 25]. However, in this project these methods were applied for the first time to the problem of QR in 2D. Before specific results for the 1D cases studied are presented in the next chapter, it is useful to give an overview of the general procedures involved in the time-dependent calculation of the reflection coefficient.

In this case the time-dependent Schödinger Equation (TDSE) needs to be solved numerically:

$$\hat{H}\psi = i\hbar\frac{\partial \psi}{\partial t} \tag{1.6}$$

where ψ is an arbitrary wave function in Hilbert space, i is the imaginary unit, $\hbar$ is the reduced Plank constant and $\hat{H} = -\frac{\hbar^2}{2m}\frac{d^2}{dx^2} + V(x)$ is the Hamiltonian operator.

For this, the Crank Nicolson (CN) finite difference scheme is applied. The CN method is a numerical algorithm for solving partial differential equations. It is particularly often

used in the solution of the heat equation, as well as the Schrödinger equation, in which its remarkable conservation properties play a central role. It is implicit and second order accurate in space and time, and guarantees an unconditional stability in the time evolution [43, 51] . It may also be regarded as an implicit Runge-Kutta scheme [10]. The major advantage of its application to the Time-Dependent Schrödinger Equation is its norm-preserving property, which guarantees, under most conditions, that the probability density function (PDF) which describes the wavepacket within the numerical box remains normalised throughout the propagation, independently of the time step chosen (see below) [43]. Furthermore, being the CN method implicit, the Courant-Friedrichs-Lewy (CFL) condition [5] [1] does not apply, so that the size of the time step chosen does not generally need to be constrained by the spatial step size and the velocity of the wave.

Eq.(1.6) has general solutions of the form:

$$\psi(\vec{r},t) = \psi(\vec{r},t_0)\exp(-\frac{i\hat{H}}{\hbar}(t-t_0)) \tag{1.7}$$

where $\vec{r}$ is a position vector and t is time.

Approximating Eq.(1.7) for an explicit finite difference method yields:

$$\psi_j^{n+1} = (1 - \frac{i\hat{H}}{\hbar}\delta t)\psi_j^n \tag{1.8}$$

whereas an implicit scheme would make use of the form:

$$(1 + \frac{i\hat{H}}{\hbar}\delta t)\psi_j^{n+1} = \psi_j^n \tag{1.9}$$

However, neither of these two differencing methods is unitary, hence none of them is intrisically norm-preserving. However, a combination of half explicit time step and half implicit time step yields Cayley's form for the finite difference approximation of the Schrödinger equation [43]:

$$(1 + \frac{i\hat{H}}{2\hbar}\delta t)\psi_{t+\delta t} = (1 - \frac{i\hat{H}}{2\hbar}\delta t)\psi_t \tag{1.10}$$

By comparing the first two terms of the Taylor expansion of both sides of Eq.(1.10) it is possible to check that this scheme is in fact accurate to second order with respect to time.

Finally, by calculating the absolute value of Eq.(1.10) the unitary property of this scheme can be verified.

---

[5]The CFL condition is a necessary requirement for the stability of explicit numerical integration schemes. In heuristic terms, it states that, in order to propagate a wave with velocity u across a spatial domain with discrete step size Δx, the time step needs to be smaller than the time taken by the wave to travel a distance Δx.

Further details on the finite differencing in 2D will be given in Sections (2.1).

The general procedure used to calculate the reflection coefficient R is the following.

An initial gaussian wavepacket is generally assumed (although any normalisable wave-form is in principle allowed), with a given initial momentum **p** and spatial spread σ_x along x (and, in the 2D case, σ_y along y). This is initially located in a given region of space, where the potential must be flat enough in order to avoid spurious scattering processes. The initial width must be small enough for the wavepacket to be contained in the numerical box within approximately 10σ. In fact, although the wave function is normalised numerically before the propagation starts, the entity of the initial state can be modified by such artificial normalisation if a significant portion of the wavepacket lies outside of the box.

In the case of interaction with an attractive surface, the incoming wave encounters a relatively sudden decrease in the potential, which causes a partial reflection of the wavepacket, as well as a partial transmission to the bottom of the potential. In the case of a singularity in the potential, this needs to be smoothly continued, since a numerical scheme cannot treat singularities. A number of continuation methods were investigated by Herwerth [28]. Finally, a parabolic continuation was chosen (see Sec. 1.4). The TDSE in Cayley's form (Eq.1.10) is thus solved (at each grid point) for the wavepacket at the next time step. At an arbitrary number of time steps, the momentum representation of the wavefunction $\hat{\psi}(\mathbf{p})$ is calculated numerically by means of a Fast Fourier Transform (FFT). The reflection coefficient R is thus computed (for the 2D case) by integrating the wavefunction across the region of interest in momentum space. This operation has to be done at an asymptotically large time, in order to ensure that the scattering process is concluded:

$$R_{t \to \infty} = \int_{P_R} \hat{\psi}(\mathbf{p}) \mathrm{d}^N \mathbf{p} \tag{1.11}$$

where P_R is the region in momentum space which contains the reflected component of the wavefunction, and N is the dimensionality of the space of interest.

As the transmitted component of the wavepacket propagates even further down the potential, its momentum increases considerably, so that it would undergo reflection as it reaches the (in our case lower) boundary of the numerical box. This unwanted reflection would not allow us to measure correctly the reflection coefficient which results from quantum reflection (because both would contribute to the amplitude of the wavefunction in momentum space), hence the wave is suppressed by means of a filtering scheme which was originally
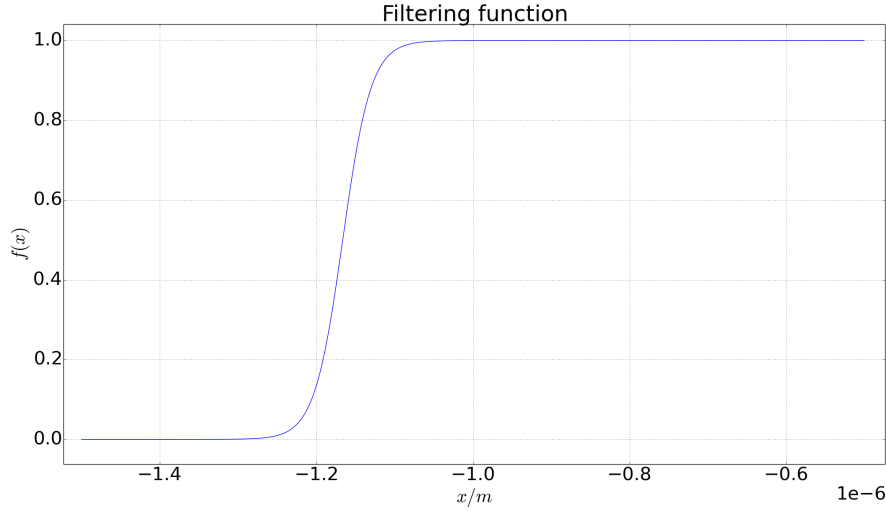
Fig. 1.2 The graph shows the filtering function which is used to absorb the transmitted component of the wavefunction as it approaches the negative edge of the numerical box. The surface is assumed to be at $x = 0$, and the left end of the numerical box is at $x = -1.5$ μm. The optimisation of the filtering function in order to avoid artificial reflections at it is still an open problem which will be subject to future studies.

developed by Herwerth [29]. Such method, which was preferred to a number of other possibilities, consists of multiplying the wavepacket by a sigmoid function of the form:

$$f(x) = \frac{1}{e^{-\frac{x-a}{d}} + 1} \tag{1.12}$$

where the coefficients a and d are determined by imposing the conditions that:

- The value of f at the lower boundary x_b of the numerical box is $f(x_b) = 10^{-8}$.

- An absorption region was defined as $x_b < x < c$, where c is an arbitrary point, which was chosen as $1\mu m$. The condition on f is thus: $|f(x) - 1| < 10^{-16}$ for $x > c$.

In practice, the wavepacket is multiplied at each position $\mathbf{r}$ by the corresponding value of the filter $f(\mathbf{r})$. The main difficulty in the design of an appropriate filter arises in avoiding artificial reflections of the wavefunction when it is absorbed. From the argument presented in Sec.(1.2) it can be inferred that this is expected to happen if the relative relative change in the De Broglie wavelength is too sudden. The filter parameters shown above were chosen by Herwerth in his 1D work [28, 29], and were thus used as a starting point for our 2D tests in matching 1D results. A plot of the numerical filter is shown in Fig.(1.2)

In order to evaluate numerically the second derivatives of the wavefunction in the Hamiltonian, a three-point approximation (see 2.3 for more details) is used. In 1D, this results in a tridiagonal structure of the Hamiltonian matrix, which is then solved via Gaussian elimination [28, 50]. To this end, the numerical routine `tridag`, available from the *Numerical Recipes* C++ library [43] was used.

Finally, it is important to specify the fact that, although the CN method is unconditionally stable [43], errors associated to finite size effects play a significant role in the propagation. Errors associated to the finite differencing in time typically cause lags in the propagation, even though the norm is preserved. On the other hand, errors due to the finite spatial step manifest themselves in the poor resolution of the potential structure and especially of fast oscillations which arise as a result of scattering processes. In particular, the latter case can ultimately lead to losses in the norm of the wavefunction.

The codes used here to perform preliminary tests with the 1D procedure were implemented by Sünderhauf [50].

1.4 Recent achievements in numerical studies of QR

As a preliminary analysis, a 1D potential step was studied numerically. This investigation enabled the detection of spurious reflections off the numerical filter. Furthermore, the reflectivity of the potential step can be proved to be larger than any other functional form for the drop in the potential at a given ratio of the energy of the incoming particle to the change in potential [24]. This preliminary numerical analysis is described in detail in Appendix A.

The treatment of QR at a one dimensional Casimir-Van der Waals potential of the form x^{-3} (see Eq. (1.3)) was originally performed by Herwerth et al. [29]. As a preliminary study, 1D results on such potential were reproduced in order to explore the parameter space in 1D, before moving to the more complex 2D case. Moreover, the reproduction of these results with our new 2D code is a necessary starting point for full 2D calculations.

Although an analytic solution is not available for such potential, two different numerical approaches are viable, and can be compared with each other in order to benchmark the propagation method:

- Integration of the time-independent Schrödinger equation given a set of known stationary boundary conditions.

- Propagation of the wavepacket by means of the time-dependent Schrödinger equation via the Crank-Nicolson scheme described in Sec. 1.3.1.

In order to avoid the singularity at $x = 0$, the potential is continued in the region $0 < x < x_0$ (where x_0 is an arbitrary continuation point which should be close enough to the surface in order for QR to occur before the wavepacket reaches the continuation point) as a parabola $V_c(x)$, which is defined by the three conditions:

1. $V_c(x_0) = V(x_0)$

2. $\left. \frac{dV_c}{dx} \right|_{x=x_0} = \left. \frac{dV}{dx} \right|_{x=x_0}$

3. $\left. \frac{dV_c}{dx} \right|_{x=0} = 0$

namely, the continuation must be smooth at x_0, and the parabola must become flat at $x = 0$. For $x < 0$, the potential remains at a constant value, which is determined automatically by the three conditions above.

The complete potential used in the 1D numerical simulations is thus:

$$V(x) = \begin{cases} -\frac{C_3}{x^3} & \text{if } x > x_0 \\ ax^2 + c & \text{if } 0 < x < x_0 \\ c & \text{if } x < 0 \end{cases} \qquad (1.13)$$

where a and c are determined by imposing the three conditions described above on the parabola (the linear term is 0 since the vertex of the parabola lies at $x = 0$). The potential is shown in Fig. 1.3. The figure includes the full potential with the repulsive regime, which is neglected in the numerical treatment, as well as the singular attractive potential and the parabolically continued form used in numerical computations. The surface is located at $x = 0$.

1.4.1   Integration of the time-independent Schrödinger equation

The aim of this method is to find, given suitable boundary conditions, a stationary solution to the time-independent Schrödinger equation:

$$\hat{H}\psi = E\psi \qquad (1.14)$$

where E is a given energy eigenvalue and ψ is a given stationary eigenstate of the Hamiltonian.

In the limit where $x \to -\infty$, the particle can be assumed to be free due to the flat shape of the potential. Therefore the wavefunction must have a plane wave form at the negative x
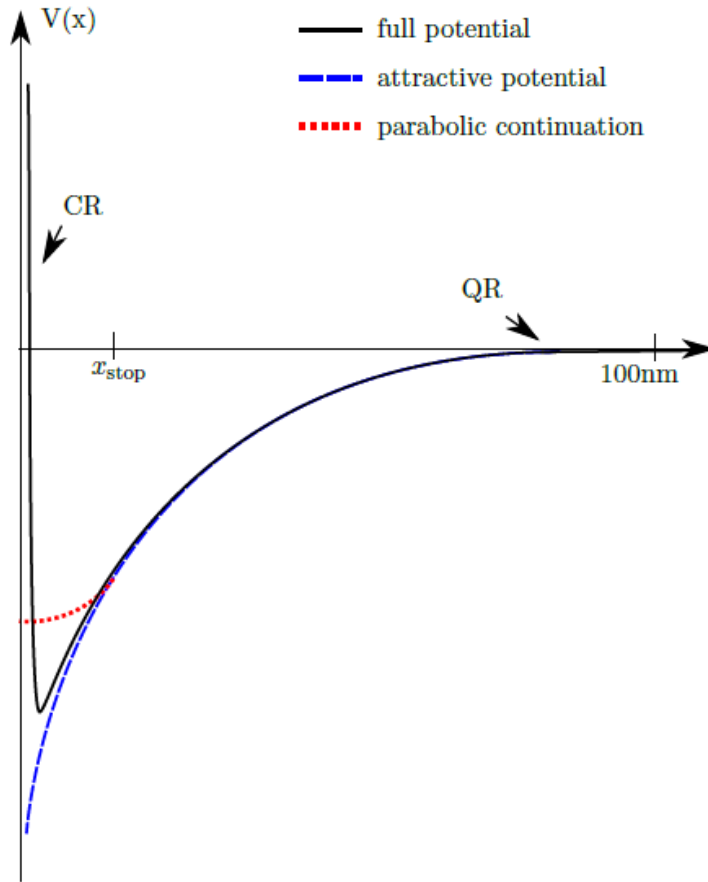
Fig. 1.3 The graph shows the potential which describes atom-surface interactions. The black curve is the full potential which includes the attractive and repulsive regimes (Eq. (1.2)). The blue curve is the attractive regime which is responsible for QR (Eq. (1.3)), and the red dotted curve is the continued potential used in numerical treatments (Eq. (1.13)). Since QR occurs when the wavepacket enters the attractive regime, the effect of repulsive interactions can be neglected since the two effects are distinct. The wavepacket is propagated from positive x towards the attractive surface. The regions where QR and CR occur are indicated (further details on this are given in the following section). The present diagram was reproduced from [50].

boundary x_m, which must be chosen such that the distance to the region where the potential changes is large compared to the local De Broglie wavelength. This results, for a particle which approaches the surface from positive to negative values of x, in a waveform:

$$\psi_{-\infty}(x_m) = u_t(x_m) = Ce^{-ik_L x_m} \tag{1.15}$$

Similarly, in the limit of $x \to \infty$, where the slope of the potential is also negligible, the expected wave form at the boundary would be:

$$\psi_{+\infty}(x) = u_i(x_M) + u_r(x_M) = Ae^{-ik_Rx_M} + Be^{ik_Rx_M} \tag{1.16}$$

where u_i and u_r are the incident (left-going) and reflected (right-going) waves, x_M is the positive edge of the numerical box, which is assumed to be much larger than zero, and x_m is its negative counterpart.

By inserting the plane wave solutions into the TISE at the two boundaries of the numerical grid, the values of k_L and k_R can be determined from the energy of the incoming particle and the potential energy as:

$$k(x) = \frac{\sqrt{2m[E - V(x)]}}{\hbar} \tag{1.17}$$

In practice, a complex amplitude C is arbitrarily chosen at x_m, and the TISE is solved up to x_M, where the continuity and differentiability conditions are imposed, thus yielding two equations for A and B. Hence, the reflection coefficient $R = \frac{|B|^2}{|A|^2}$, can then be computed by solving the two coupled equations (and similarly for the trasmission).

The Python code used to perform this task was written by Herwerth [28]. The numerical adaptive integrator `odeint` from the *SciPy* software package was used in order to solve numerically the TISE.

1.4.2   Results of preliminary 1D investigations

The time-independent method was applied to a particle moving with velocity $v = -2ms^{-1}$, in a spatial domain $-1.5 \ \mu m < x < 5.5 \ \mu m$. Results were computed for $1.5 \times 10^{-11} \ m < x_0 < 2.0 \times 10^{-8} \ m$. The outcome was then compared to the time-dependent result, which was run with the same physical parameters, for values of the continuation point $1.0 \times 10^{-10} \ m < x_0 < 9.0 \times 10^{-9} \ m$ at different values of the spatial step-size. The time-step size was always kept within a factor of two (in internal units) of the spatial step-size. This was found to be generally a safe parameter choice.

A typical wavepacket propagation is shown in Fig.(1.4).

As the particle starts propagating in the negative x direction, the reflectivity should only be measured as a result of the finite spread in momenta. However, a finite background noise of order $\sim 10^{-18}$ is always present in the reflection, which, as shown by Sünderhauf [50], cannot be caused by the Heisenberg Uncertainty principle, but it arises from numerical noise due finite size effects.
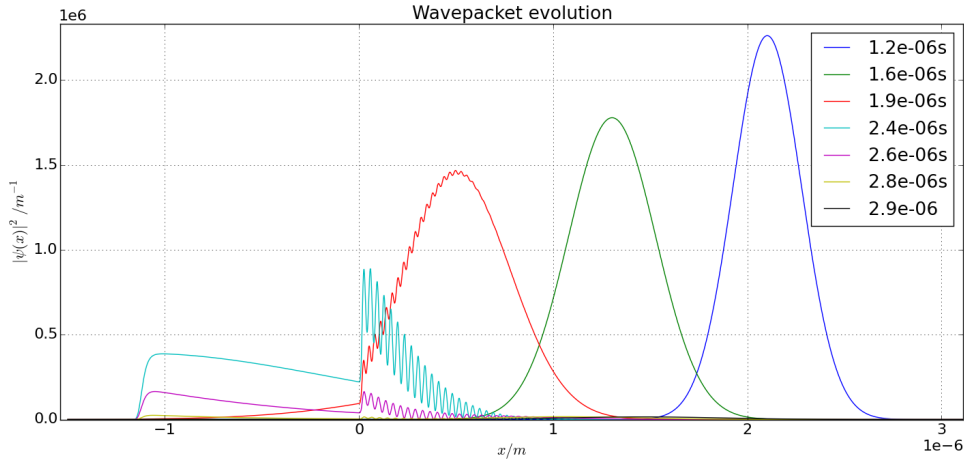
Fig. 1.4 In this graph, the square modulus of the wavefunction is shown at different times for a typical wavepacket propagation in coordinate space. The wavepacket starts at a position far from the attractive potential (such that $V(x - \sigma_x) \simeq 0$). As it reaches the region where $x \approx 0.5$ μm, it undergoes reflections, which result in abrupt oscillations. The fact that QR occurs at this position justifies the choice of continuation points $x_0 \leq 10$ nm, since QR has already happened when the wavepacket reaches that regime. The wavepacket is partially transmitted to the bottom of the potential. The transmitted component is then absorbed artificially by the filter. The reflected component, which travels back in the positive x direction, is not evident at this scale in coordinate space.

The results for the time-independent and time-dependent methods are shown in Fig. 1.6 for different values of the continuation point x_0.

The plot clearly shows that the introduction of an artificial continuation point induces an oscillatory behaviour in the reflectivity with respect to x_0. It was found by Herwerth, that the wavelength of these oscillations increases as $x_0^{3/2}$ [29]. However, the oscillations vanish as the continuation distance tends to 0. The importance of this finding is central to the final aim of this project. In fact, as can be seen from the graph, smaller continuation points require a higher number of gridpoints in order to resolve the potential at small distances from the singularity. However, this result shows that an averaging process can be performed, in order to obtain the correct value of the reflection coefficient while keeping the continuation point relatively far from the singularity. This fact will be crucial in order to reduce computational costs once a second dimension is introduced.

As opposed to this result, it can be clearly seen that the reflectivity is very sensitive to the shape of the potential in the regime $E \sim V(x)$, which occurs at farther distances from the singularity. In fact, the classical kinetic energy of the incoming particle is of order $\frac{1}{2}mv^2 \sim 10^{-26} J$. The absolute value of the potential energy at $x_0 \sim 10^{-8} m$, where the
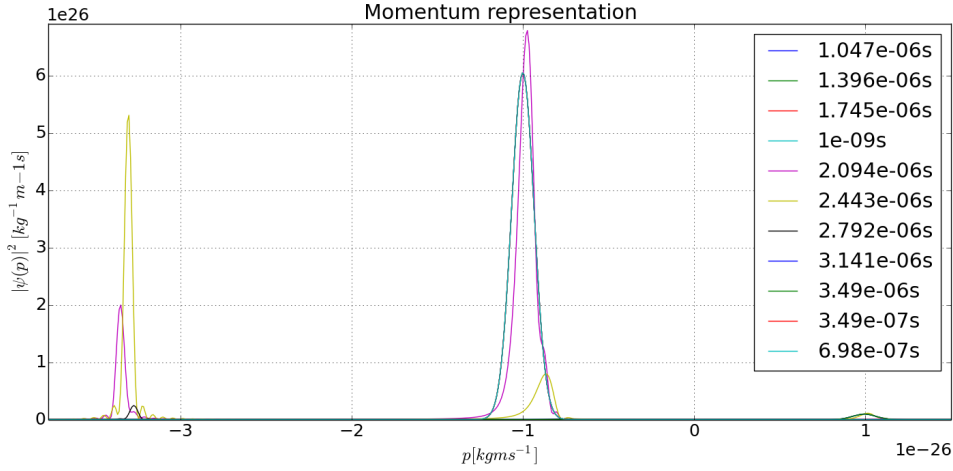
Fig. 1.5 The graph shows the typical evolution of the square modulus of the wavefunction in momentum space. The initial momentum of the particle is $p \approx -10^{-26}$ kg m s^{-1}. The reflected component, which is the smaller peak at $p \approx -10^{-26}$ kg ms^{-1} has the same modulus of the momentum, as it has to be for an elastic collision. The negative momenta, which correspond to the transmitted component of the wavepacket, are absorbed after a certain time (namely, when such wave reaches the numerical filter).

oscillations reach their maximum amplitude, is of order $|V| \sim \frac{C_3}{10^{-24}} \sim 10^{-26}$, which is fully consistent with the theory presented in Sec.1.2.

It can be shown [29] that, for $x_0 > 10^{-8}$, the oscillatory behaviour of R breaks down, and the reflection coefficient tends to 0. This result is expected, since the potential would then not become steep enough, and the conditions for the semiclassical approximation to hold would be fulfilled.

Another conclusion which can be drawn from Fig. 1.6 is the behaviour of R as the continuation point decreases at a fixed spatial resolution. In fact, as the potential becomes too steep to be effectively resolved with a given spatial step, the reflectivity tends to one. This result is expected from the limiting case of a potential step described in Appendix A. Although it can be interpreted physically, such behaviour is not controlled neither predictable with our current means, but it is merely a result of the bad resolution of the potential landscape. This fact showed that the uncontrolled increase of the reflection coefficient to one is a systematic error due to the insufficiently dense sampling of the potential.

Fig. 1.6 has a remarkable importance in the transition to 2D systems. In fact, the more reliable time-independent results provide a safe way of checking the regimes where the time-dependent scheme works correctly. The latter can then be generalised to 2D systems for potentials which couple the two dimensions. In practice, 1D studies allow us to choose
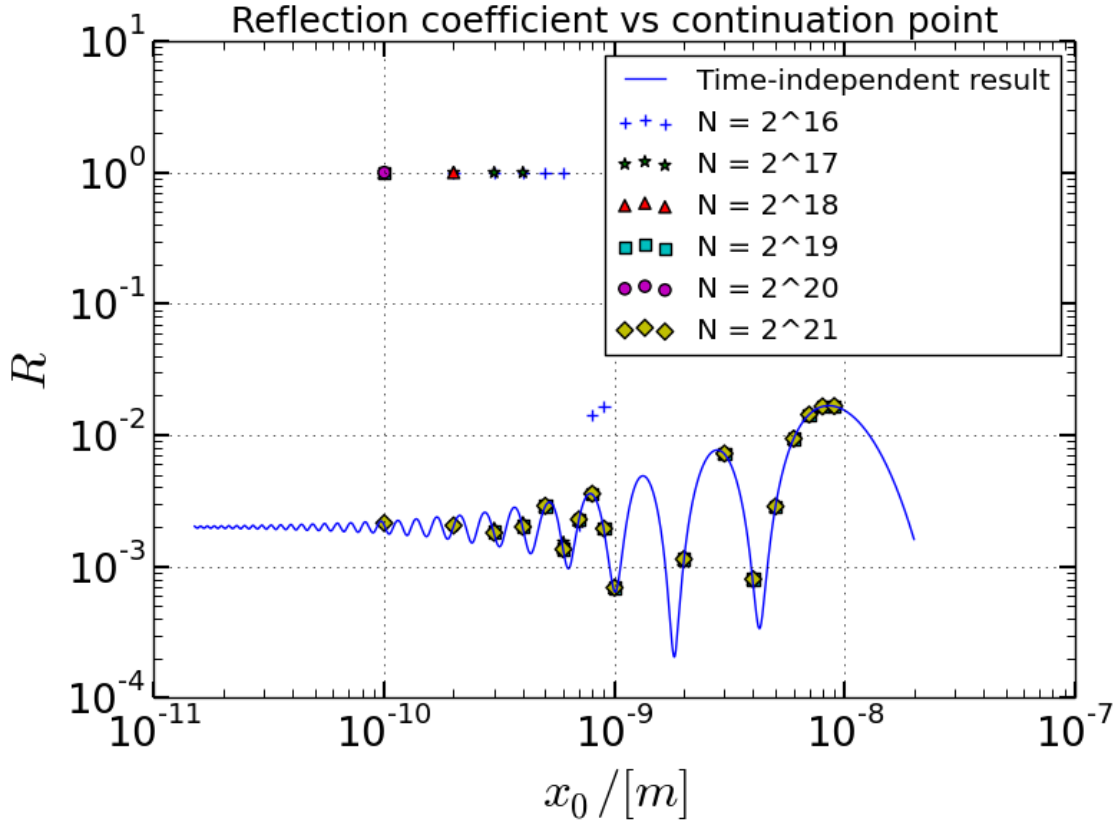
Fig. 1.6 Comparison of the time-dependent and time-independent results for R in 1D as a function of the continuation point x_0. The oscillation is an artificial effect generated by the introduction of the characteristic length x_0 at which the potential is continued. As shown by Herwerth et al. [28, 29] taking the average over the x_0 domain yields the limiting value of the reflection coefficient for the complete potential. Note that the datapoints for lower precision are hidden by higher precision ones until they diverge as x_0 becomes too close to the singularity. A continuation point $x_0 \simeq 0.1$ *nm* could only be handled by using 2^{21} gridpoints, while $x_0 \simeq 9$ *nm* could be handled by using any number of gridpoints larger or equal to 2^{16}.

accurately the optimal number of gridpoints for a given continuation point x_0, which would be more complicated for 2D codes. In fact, since the numerical scheme could fail as a result of insufficient grid sampling along any of the two dimensions, the cause for failure cannot be traced back easily as in 1D treatments. Clearly, couplings between the two dimensions would add additional difficulties to this problem.

Similarly to R, the relative errors $\frac{\Delta R}{R}$ between the time-independent and time-dependent methods oscillate between values of order 10^{-1} and 10^{-3}, as shown by Herwerth [28].

However, given the high sensitivity of QR to the shape of the effective shape of the potential, this error size is remarkably good, especially since the relative error in QR experiments performed with the ABSE method are never smaller than 10^{-2} [12].

Chapter 2

Numerical background and implementation

The generalisation of the 1D methods to 2D results in much higher computational costs, thus making a high level of optimisation necessary both in the algorithms used and in the choice of parameters.

In this chapter the numerical methods used for the propagation of wavepackets in 2D are discussed in detail, whereas the next chapter gives an overview of the new results of the various tests which were performed using these 2D methods.

To begin with, the 2D generalisation of the Crank-Nicolson scheme introduced in Chapter 1 is presented. The relationship between the structure of the Hamiltonian matrix and the mapping of the discretised wavefunction $\psi(x,y)$ on the numerical grid is discussed. Finally, the procedures used to solve the TDSE are explained, as well as a theoretical estimate of the computational costs associated with them.

2.1 Wavefunction storage and Hamiltonian matrix

The structure of the Hamiltonian matrix is intimately related to the way in which the components of the two-dimensional discretised wave function ψ are indexed.

The 2D wavefunction is stored as a 1D vector. Therefore, a mapping from the x-y plane onto the components of the discretised wavefunction is necessary. Two different mapping methods for the components of the ψ vector were proposed and preliminarily investigated by Sünderhauf [50]. The first, "by columns", consists of keeping one of the two indices constant, while letting the second index map all corresponding components in the other dimension. The second method, "by diagonals", consists of mapping the elements in such an order, that

the sum of the indices is constant. This can be most easily visualised by starting at one of the corners of the numerical grid, and subsequently looping through inner diagonals. The two cases are shown in formulae (2.1).

$$
\vec{\psi}_{\mathbf{c}} = \begin{pmatrix} \psi_{0,0} \\ \psi_{0,1} \\ \vdots \\ \psi_{0,n_y-1} \\ \psi_{1,0} \\ \psi_{1,1} \\ \vdots \\ \psi_{n_x-1,n_y-1} \end{pmatrix} \qquad \vec{\psi}_{\mathbf{d}} = \begin{pmatrix} \psi_{0,0} \\ \psi_{1,0} \\ \psi_{0,1} \\ \vdots \\ \psi_{i,0} \\ \vdots \\ \psi_{i-j,j} \\ \vdots \\ \psi_{n_x-1,n_y-1} \end{pmatrix} \tag{2.1}
$$

The Hamiltonian matrices corresponding to each indexing method were studied by Sünderhauf [50], who showed that in both cases the matrices would (without periodic boundary conditions) be banded, and proved that the size of the band could not be reduced further than n_y, independently of the indexing method used. Nevertheless, the classical mapping by columns results in a more regular matrix structure[1], which is shown in Fig. 2.1.

The time-independent Hamiltonian operator in 2D reads [26]:

$$
\hat{H}(x,y) = -\frac{\hbar^2}{2m}\left(\frac{\partial^2}{\partial x^2} + \frac{\partial^2}{\partial y^2}\right) + \hat{V}(x,y) \tag{2.2}
$$

The second partial derivatives of $\psi(x,y)$ at each grid point (i,j) with respect to x and y are evaluated via three-point approximations, such that:

$$
\left.\frac{\partial^2 \psi}{\partial x^2}\right|_{x_i,y_j} \simeq \frac{\psi_{i-1,j}}{\delta x^2} - 2\frac{\psi_{i,j}}{\delta x^2} + \frac{\psi_{i+1,j}}{\delta x^2} \tag{2.3a}
$$

$$
\left.\frac{\partial^2 \psi}{\partial y^2}\right|_{x_i,y_j} \simeq \frac{\psi_{i,j-1}}{\delta y^2} - 2\frac{\psi_{i,j}}{\delta y^2} + \frac{\psi_{i,j+1}}{\delta y^2} \tag{2.3b}
$$

where δx and δy are the finite spatial steps in the respective dimensions.

---

[1]In numerical analysis jargon, such matrix structure is called "tridiagonal with fringes" [43].

$$\begin{pmatrix} \begin{array}{ccc|ccc|ccc|ccc} d_{x_1,y_1} & \mu_y & & \mu_x & & & & & \\ \mu_y & d_{x_1,\dots} & \mu_y & & \mu_x & & & & \\ & \mu_y & d_{x_1,y_m} & & & \mu_x & & & \\ \hline \mu_x & & & d_{x_2,y_1} & \mu_y & & \mu_x & & \\ & \mu_x & & \mu_y & d_{x_2,\dots} & \mu_y & & \mu_x & \\ & & \mu_x & & \mu_y & d_{x_2,y_m} & & & \mu_x \\ \hline & & & \mu_x & & & d_{\dots,y_1} & \mu_y & & \mu_x \\ & & & & \mu_x & & \mu_y & d_{\dots,\dots} & \mu_y & & \mu_x \\ & & & & & \mu_x & & \mu_y & d_{\dots,y_m} & & & \mu_x \\ \hline & & & & & & \mu_x & & & d_{x_n,y_1} & \mu_y & \\ & & & & & & & \mu_x & & \mu_y & d_{x_n,\dots} & \mu_y \\ & & & & & & & & \mu_x & & \mu_y & d_{x_n,y_m} \end{array} \end{pmatrix}$$

Fig. 2.1 Simplified representation of the matrices involved in the two sides of Equation (2.5). The non-zero components are given as d_{x_i,y_j} for the diagonal elements and μ_x, μ_y for the terms resulting from horizontally and vertically adjacent grid points used in the three-point approximation, respectively. Each block in the matrix indicates one column (at fixed x) on the grid.

Hence the resulting finite difference Schrödinger equation in Cayley's form (Eq.(1.10)) is approximated as:

$$\left[1 + \frac{\hbar^2}{2m}\left(\frac{\partial^2}{\partial x^2}\bigg|_{x_i,y_j} + \frac{\partial^2}{\partial y^2}\bigg|_{x_i,y_j}\right) + V(x_i,y_j)\right]\psi_{i,j}^{n+1} = \left[1 - \frac{\hbar^2}{2m}\left(\frac{\partial^2}{\partial x^2}\bigg|_{x_i,y_j} + \frac{\partial^2}{\partial y^2}\bigg|_{x_i,y_j}\right) + V(x_i,y_j)\right]\psi_{i,j}^{n}$$

$$(2.4)$$

where the partial derivatives are evaluated according to Eqs.(2.3), the indices i and j refer to gridpoints in the x and y dimension respectively, and n is the time index.

Equation (2.4) represents a set of $n_x \times n_y$ linear equations. Neglecting boundary conditions, each point in the grid results, because of the three-point approximation, in a linear equation which couples to the ones for its neighbouring grid points.

Higher order approximations for the second derivatives can be easily implemented by including additional terms in the Hamiltonian matrix, which would result in a higher number of terms in each equation. The five-point approximation was implemented by

Herwerth [29] for the 1D case. However, in that context the improvement given by the higher order approximation was not found to be significant enough to justify the additional computational costs, which would arise as a consequence of the increased size of the blocks in the Hamiltonian matrix, as described below.

Such system of linear equations can then be conveniently written in matrix form as:

$$\mathscr{A}_+ \vec{\psi}^{n+1} = \mathscr{A}_- \vec{\psi}^n \tag{2.5}$$

where the matrices of the coefficients $\mathscr{A}_+$ and $\mathscr{A}_-$ are represented graphically in Fig. (2.1), and their non-zero elements are defined as:

$$d_{i,j} = 1 \pm \left(\frac{\hbar^2}{m\delta x^2} + \frac{\hbar^2}{m\delta y^2} + V_{i,j} \right) \frac{\delta t}{2\hbar} \tag{2.6a}$$

$$\mu_x = \mp i \frac{\hbar^2}{2m\delta x^2} \frac{\delta t}{2\hbar} \tag{2.6b}$$

$$\mu_y = \mp i \frac{\hbar^2}{2m\delta y^2} \frac{\delta t}{2\hbar} \tag{2.6c}$$

The upper sign in Eqs.(2.6) corresponds to the left hand side (LHS) matrix of Eq.(2.4) while the lower sign corresponds to its right hand side (RHS).

Hence, the only non-zero components of the matrices 2.1 are the following:

1. d_{x_i, y_j} are the diagonal elements, which contain the potential at the different grid points.

2. μ_x is the off-diagonal element which is results from the coupling between adjacent points in x on the grid in the three-point approximation. It is constant over the whole x-domain and depends only on the time step, the spatial step along the *x* direction, the mass of the particle.

3. μ_y is the corresponding off-diagonal element along *y*, and has the same properties of μ_x if *x* is replaced by *y*.

2.1.1 $\mathscr{L}\mathscr{L}^T$ decomposition

Since the matrix described above is a symmetric and positive-definite, it can be decomposed via Cholesky, or $\mathscr{L}\mathscr{L}^T$, decomposition. This consists of rewriting the matrix $\mathscr{A}$ as the product of a lower triangular matrix $\mathscr{L}$ and its transpose $\mathscr{L}^T$. Such procedure is a factor of two more efficient than a standard $\mathscr{L}\mathscr{U}$ decomposition [43], which is crucial for our

purposes, especially in terms of memory use. As shown later in this chapter, such matrix decomposition allows for a fast procedure for solving Eq.(2.5) for $\psi_{t+\delta t}$.

It can easily be proved [30] that the matrix $\mathscr{L}$ resulting from $\mathscr{L}\mathscr{L}^T$ decomposition of a banded matrix is also banded with the same band size (namely n_y). However, $\mathscr{L}$ is not sparse, thus making it necessary to save its elements. The storage of $\mathscr{L}$ is the primary reason for the large memory requirements of our method.

Thus, in order to minimise the number of elements to save, only the elements which belong to the non-zero band are saved. Therefore, the matrix is conveniently stored as an array of vectors of variable lengths, each storing a diagonal of the band. A natural indexing method for the matrix elements is evidently by diagonals. Hence, in our routines the first index denotes the distance from the main diagonal, while the second denotes the column, as shown in Fig. 2.2. Hence, the memory needed to store the necessary information contained in $\mathscr{L}$ is of the order of $(n_x \times n_y) \times n_y$, namely, the length of the main diagonal times the width of the matrix band. The memory cost is clearly quadratic in n_y and linear in n_x. This asymmetry plays a significant role in the choice of dimensions when applying this method to the modeling of a physical problem.

The memory M and runtime T required for a generic $\mathscr{L}\mathscr{L}^T$ decomposition as a function of the number of spatial grid points was tested in detail by Sünderhauf [50], who obtained an estimate $M \approx (14.02 + 1.86 \times 10^{-5} \times n_x \times n_y^2)$ MB for the memory required to store the $\mathscr{L}$ matrix and a CPU time $T \approx (6.82 \times 10^{-8} n_x \times n_y^3)s$. The memory constraint is clearly a limiting factor, since machines with more than 256 GB of memory are not commonly available, whereas CPU time could, in principle, be improved via further optimisation. However, since CPU time grows significantly before memory costs become too large, the memory effectively used in preliminary tests was always less than 10 GB.

The standard algorithm used to perform $\mathscr{L}\mathscr{L}^T$ decomposition is the following:

$$\mathscr{L}_{ii} = \left(a_{ii} - \sum_{k=0}^{i-1} \mathscr{L}_{ik}^2 \right)^{1/2} \tag{2.7a}$$

$$\mathscr{L}_{ij} = \frac{1}{\mathscr{L}_{ii}} \left(a_{ij} - \sum_{k=0}^{i-1} \mathscr{L}_{ik}\mathscr{L}_{jk} \right) \tag{2.7b}$$

where i indicate the rows and j the columns of the matrices, and a_{ij} are the elements of the original matrix. This procedure needs to be performed by columns, since each step requires a knowledge of the elements which have been previously calculated [43].

In order to fully exploit the symmetries of the matrix under consideration, optimised versions of matrix-vector operations were implemented, which take into account the banded structure of the matrix, thus performing non-zero operations only.

$$\begin{pmatrix}
\boxed{\begin{matrix} L_{0,0} \\ L_{1,0} \quad L_{0,1} \\ L_{2,0} \quad L_{1,1} \quad L_{0,2} \\ L_{...,0} \quad L_{2,1} \quad L_{1,2} \quad L_{0,...} \end{matrix}} \\
L_{n_y,0} \quad L_{...,1} \quad L_{2,2} \quad L_{1,...} \quad \boxed{\begin{matrix} L_{0,n_y} \\ L_{1,n_y} \quad L_{0,...} \\ L_{2,n_y} \quad L_{1,...} \quad L_{0,...} \\ L_{...,n_y} \quad L_{2,...} \quad L_{1,...} \quad L_{0,...} \end{matrix}} \\
\end{pmatrix}$$
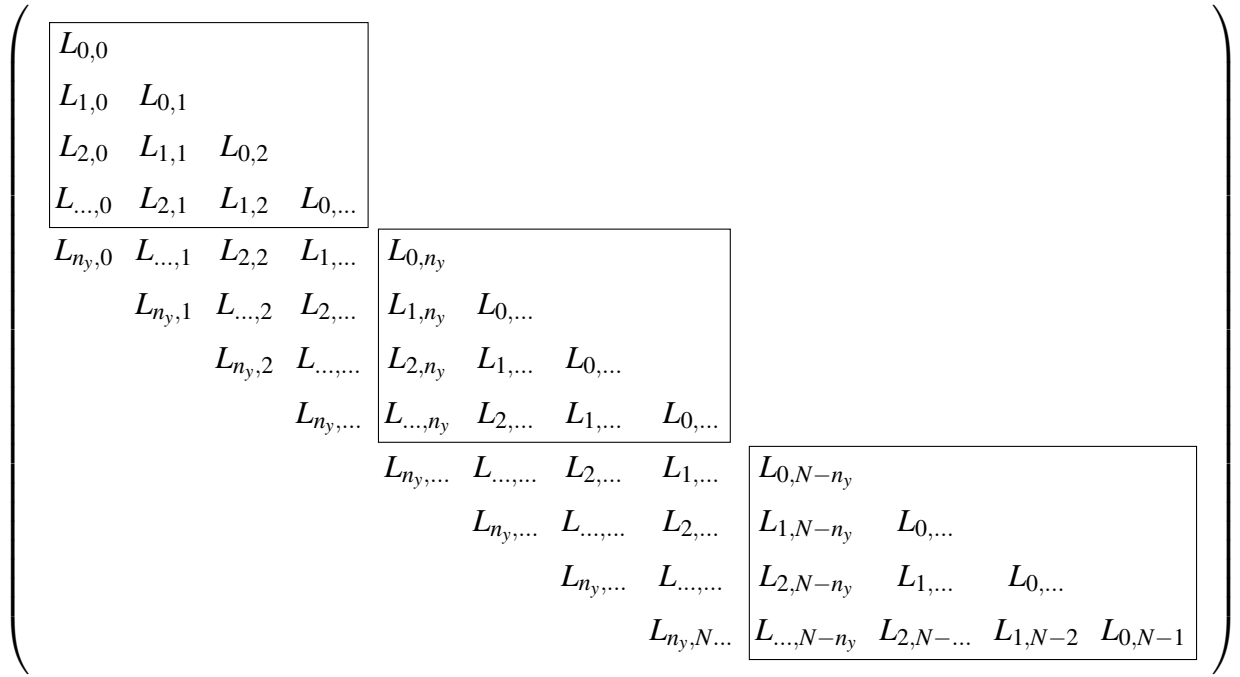
Fig. 2.2 The structure and indexing of the $\mathscr{L}$ matrix. Each diagonal is saved in a separate vector, whose length depends on the distance from the main diagonal. Here N corresponds to the total number of gridpoints $n_x \times n_y$.

Once the routine was implemented, its correctness was checked numerically by recalculating the original matrix by means of a standard matrix multiplication. This also allowed us to monitor the typical size of numerical errors, which, for a flat potential, was always found to be within two orders of magnitude of machine precision. Nevertheless, this estimate would need to be done for each individual simulation, since it depends on the spatial and temporal step sizes (hence on the size of the matrix), as well as the potential in question.

2.1.2 Periodic Boundary Conditions

It was shown in the previous section how the computational costs increase very differently depending on the dimension in which the number of gridpoints is increased. This fact makes our method ideal in cases where the size of the numerical box is very different in the two dimensions, although it places stringent limits to the number of gridpopints in y. Nevertheless, all is not lost. If periodic periodic boundary conditions (PBC) are introduced along y, the configuration of the elements in the $\mathscr{A}$ matrix is changed as shown in Fig.(2.3). The additional μ_y elements which enable the application of PBC along y must be located

$$
\begin{pmatrix}
d_{x_1,y_1} & \mu_y & & \mu_y & \mu_x & & & & & & & \\
\mu_y & d_{x_1,y_2} & \mu_y & & & \mu_x & & & & & & \\
& \mu_y & d_{x_1,y_{...}} & \mu_y & & & \mu_x & & & & & \\
\mu_y & & \mu_y & d_{x_1,y_{n_y}} & & & & \mu_x & & & & \\
\mu_x & & & & d_{...,y_1} & \mu_y & & \mu_y & \mu_x & & & \\
& \mu_x & & & \mu_y & d_{...,y_2} & \mu_y & & & \mu_x & & \\
& & \mu_x & & & \mu_y & d_{...,...} & \mu_y & & & \mu_x & \\
& & & \mu_x & \mu_y & & \mu_y & d_{...,y_{n_y}} & & & & \mu_x \\
& & & & \mu_x & & & & d_{x_{n_x},y_1} & \mu_y & & \mu_y \\
& & & & & \mu_x & & & \mu_y & d_{x_{n_x},y_2} & \mu_y & \\
& & & & & & \mu_x & & & \mu_y & d_{x_{n_x},...} & \mu_y \\
& & & & & & & \mu_x & \mu_y & & \mu_y & d_{x_{n_x},y_{n_y}}
\end{pmatrix}
$$

Fig. 2.3 Structure of $\mathscr{A}$ with periodic boundary conditions in both dimensions. The elements at the corners of the rectangular boxes are responsible for periodic boundary conditions in y, while the diagonals of elements at the opposite corners of the matrix yield periodic boundary conditions in x. The base of the triangles formed by the such diagonals and the edges of the matrix is n_y, while the bulk of the matrix, which only contains zeroes, lies (both in the upper-right and lower left sides of the matrix) between the diagonals formed by the μ_x elements, and its size is, to highest order, $(n_y - 2) \times n_x/2$ on each side.

at the top-right and bottom-left corners of each rectangular box in Fig. 2.1. On the other hand, PBC along x require additional elements along two diagonals n_y elements far from the corners of the $\mathscr{A}$ matrix, which results in elements far outside of the non-zero band.

Nevertheless the additional elements which account for PBC in y fall within the non-zero band of the matrix. As discussed in the previous section, $\mathscr{L}\mathscr{L}^T$ decomposition of a banded matrix preserves the size of the band, although the lower decomposition is no longer sparse, so that its size is responsible for most of the computational costs. Therefore it is negligibly expensive to introduce PBC in the y dimension, while in the case of PBC along x the size of the banded $\mathscr{L}$ matrix would increase by a factor of order $n_x \times (n_y - 2)/2$, thus making the whole calculation unfeasible.

Therefore, it is evident that our method has the ideal features to be applied to the physical problem of QR at a periodically corrugated surface. In fact a long but not periodic box is needed in such case along the x axis, along which the particle approaches the surface, while

the periodicity of the potential along the *y* axis enables the use of PBC without a significant loss of information.

Clearly, periodic boundary conditions result in the wavepacket to interfere with itself, which would be equivalent to having a beam of atoms which approach the surface at the same incidence. This problem is not discussed in the present thesis, and will be treated in future developments of this project.

2.2 Propagation procedure and computational costs

The aim of our algorithm is to solve Eq.(2.5) for $\vec{\psi}_{t+\delta t}$. To this end, two approaches can be taken:

1. The matrix $\mathscr{A}^{-1}$ is computed by matrix inversion. This could then be saved and used iteratively (since the Hamiltonian is time-independent) to obtain $\vec{\psi}_{t+\delta t}$ from $\vec{\psi}_t$ by mere matrix multiplication at each time step.

2. The $\mathscr{L}$ matrix is used to propagate the wavepacket directly by means of a forward and a backward substitution at each time step.

The following analyses show the operations which are necessary to solve Eq.(2.5) via the two different approaches. The memory requirement and the number of operations associated to each of them are considered, in order to motivate our choice.

2.2.1 Matrix inversion

The following equation needs to be solved:

$$\mathscr{A}\mathscr{A}^{-1} = \mathbb{I} \tag{2.8}$$

for $\mathscr{A}^{-1}$, where the matrix $\mathscr{A}$ has already been decomposed into the product $\mathscr{L}\mathscr{L}^{\mathscr{T}}$. To this purpose, the inverse L^{-1} is initially computed, which solves the equation:

$$\mathscr{L}\mathscr{L}^{-1} = \mathbb{I} \tag{2.9}$$

The extent of such calculation, as well as the storage needed, can be significantly reduced with the aid of the following lemma [30]:

Lemma: *The inverse of a lower triangular matrix is a lower triangular matrix.*

This statement can be easily proved by considering, from the first row on, the elements of Eq.(2.9) in the upper-right region of $\mathbb{I}$.

As a result, the memory required for the storage of $\mathscr{L}^{-1}$ is, to highest order, $n_x \times n_y^2$.

The operations required to compute $\mathscr{L}^{-1}$ are, approximately $\frac{(n_x^2 \times n_y^3)}{2}$ additions, $\frac{(n_x^2 \times n_y^3)}{2}$ multiplications, and $\frac{(n_x^2 \times n_y^2)}{2}$ divisions.

Hence, the equation:

$$\mathscr{L}^T \mathscr{A}^{-1} = \mathscr{L}^{-1} \tag{2.10}$$

needs to be solved in order to obtain the inverse $\mathscr{A}^{-1}$. needed to propagate ψ over time. This operation results generally in a full matrix $\mathscr{A}^{-1}$ which needs to be stored. Therefore, the number of elements to store would be $(n_x \times n_y)^2$.

In order to obtain $\mathscr{A}^{-1}$ the estimated number of operations required is: $\frac{(n_x \times n_y)^3}{2}$ additions $\frac{(n_x \times n_y)^3}{2}$ multiplications and $\frac{(n_x \times n_y)^2}{2}$ divisions.

The total number of elements to store is then of order $(n_x \times n_y)^2$, while the total number of operations (neglecting the difference in computational costs between the different operations) would be of order $(n_x \times n_y)^3$.

2.2.2 Direct propagation of the wavepacket

In this case, the aim is to solve Eq.(2.5) directly. The matrix $\mathscr{A}_+$ has been decomposed into the product $\mathscr{L}\mathscr{L}^T$. Hence, the matrix equation can be rewritten as:

$$\mathscr{L}(\mathscr{L}^{\mathscr{T}} \vec{\psi}_{t+\delta t}) = (\mathscr{A}_- \vec{\psi}_t) \tag{2.11}$$

Since the matrix $\mathscr{A}_-$ has the sparse structure shown in Fig.(2.1) the RHS of Eq.(2.11) is efficiently calculated by performing only non-zero operations, which results in five multiplications and five additions per grid point (ignoring the special cases at the x-boundaries).

The LHS of Eq.(2.11) can be rewritten in terms of the unknown vector $\vec{y} = \mathscr{L}\vec{\psi}_{t+\delta t}$ as:

$$\mathscr{L}\vec{y} = \vec{b} \tag{2.12}$$

where $\vec{b}$ denotes the RHS of Eq.(2.11), which is known.

Thus, being $\mathscr{L}$ a lower triangular banded matrix, Eq.(2.12) can be efficiently solved for $\vec{y}$ via forward substitution [43]. The standard procedure for forward substitution was adapted to the banded structure of $\mathscr{L}$ in order to compute only non-zero operations.

Finally, the upper triangular banded structure is exploited in order to solve efficiently the equation:

$$\mathscr{L}^T \vec{\psi}_{t+\delta t} = \vec{y} \tag{2.13}$$

for $\vec{\psi}_{t+\delta t}$ via back-substitution.

Since no matrices other than $\mathscr{L}$ need to be saved with this method, the memory cost associated to it is trivially given by the size of the $\mathscr{L}$ matrix, which is lower triangular and banded with width n_y. Hence it is $\frac{n_x \times n_y^2}{2}$.

The number or operations required to perform forward (and similarly backward) substitution is $n_x \times n_y^2$ additions, $n_x \times n_y^2$ multiplications and $n_x \times n_y$ divisions, which, by neglecting the difference in computational costs of the individual types of operation gives a total number of operations of order $2n_x \times n_y^2$.

The convenience of the latter method is evident, and it originates from the high computational costs associated with matrix-matrix operations needed for matrix inversion, while in the second case only matrix-vector operations are performed.

Furthermore, the memory requirement will be extremely lower than in the former case, since no full matrix needs to be saved. In fact, such matrix would have a size of order $n_x^2 \times n_y^2$, namely a factor of n_x higher than in the case of direct propagation. This would make the former method in any case unfeasible.

Chapter 3

Results of 2D tests

In order to test the algorithms which were discussed in the previous section, a number of preliminary tests were performed on well known potential structures. In particular, applying our methods to the case of a free particle, as well as the simple harmonic oscillator (SHO) potential, allowed us to compare our numerical results to exact analytical calculations.

3.1 Two-dimensional propagation tests

Initially our 2D code was tested along each dimension individually by setting to 1 the number of gridpoints in the other dimension. Only a few minor changes in the code were necessary in order to allow such tests to be performed. Such need was due to the high level of optimisation of our numerical procedures for 2D problems, which allowed us to reduce the number of checks performed in critical sections of our subroutines. However 1D results can be reproduced via truly 2D propagation as follows.

Consider a separable potential in a cartesian grid:

$$V(x,y) = V_a(x) + V_b(y) \qquad (3.1)$$

The solution to the time-independent Schrödinger equation for such a potential can be generally written as a product [44]:

$$\psi(x,y) = \psi_a(x)\psi_b(y) \qquad (3.2)$$

Hence, the square modulus $|\psi(x,y)|^2$ of the wavefunction can be integrated along one of the two dimensions to obtain the column density $|\psi(x_i)|^2$, where the notation x_i denotes either of the x or y dimension, in order to observe the effect of each part of the potential separately.

Thus, 1D results can be observed by studying 2D separable potentials, and compared to analytical calculations for integrable 1D potentials.

3.1.1 Free particle propagation

The propagation of a free Gaussian wavepacket with an initial spread $\Delta_x(0)$ can be solved analytically [7], and the result is still a gaussian function, whose standard deviation evolves in time according to:

$$\Delta_x(t) = \Delta_x(0)\sqrt{1 + \frac{\hbar^2 t^2}{4m^2\Delta_x(0)^4}} \tag{3.3}$$

Therefore, in order to compare the numerical evolution of the free wavepacket with its analytical prediction, its spread is measured during propagation, and the numerical values thus obtained are compared to the analytical predictions.

The results showed a match of the analytical results with a typical relative deviation of order 10^{-4}.

The norm was measured during the propagation at all times, and it is preserved within a maximum relative error of order 10^{-13}.

The dependence of the results on the number of gridpoints was found to be extremely weak, as expected by the fact that no potential landscape needs to be resolved.

3.1.2 Simple harmonic oscillators

In order to test the methods on analytically solvable potentials, the propagation of eigenstates of one-dimensional oscillators was tested, and their dynamics was investigated and compared to the analytical results.

The 1D potential for this system reads:

$$V(x) = \frac{1}{2}m\omega^2(x - x_0)^2 \tag{3.4}$$

where m is the mass of the particle, *omega* is the angular frequency of the oscillator, and x_0 is the abscissa of the axis of symmetry of the oscillator. Furthermore, the following characteristic quantities can be defined for the oscillator:

- The ground state energy $E_0 = \frac{\hbar\omega}{2}$ defines the energy scale of the system.

- The oscillator length $a = \sqrt{\frac{\hbar}{m\omega}}$ is defined such that $V(a) = \frac{\hbar\omega}{2} = E_0$, i.e. the ground state energy of the oscillator. It defines the characteristic length scale of the system.

- The period of the oscillator $T = \frac{2\pi}{\omega}$, which defines the characteristic time scale of the system

The functional form of the ground state of the SHO is a Gaussian [26]

$$\psi_0(x) = A_0 e^{-x^2/2a^2} \tag{3.5}$$

where A_0 is a normalisation constant.

Once the wavefunction was normalised on the numerical grid, its propagation was run, in order to observe the dynamics of the state. The result is shown in Fig. 3.1. The form of the ground state is clearly preserved during the propagation.

Furthermore, the deviations from the exact state were observed by looking at the maximum of the column density of the ground state and the result is shown in Fig. 3.2. It was observed that oscillatory deviations take place as a result of finite size errors in the state. These deviations, whose relative size is of order 10^{-4}, oscillate at the characteristic frequency of the oscillator. Furthermore, oscillations were observed at the characteristic frequency by propagating a slightly displaced gaussian function.
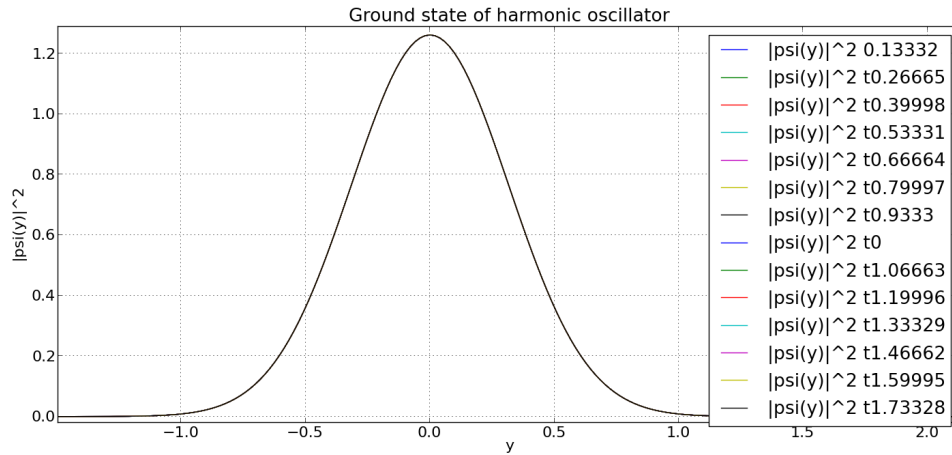
Fig. 3.1 The graph shows the confinement along y of a particle in the ground state of a simple harmonic oscillator potential. This test was performed using 2^{10} gridpoints in y. The oscillator length $a = 10$ in internal units.

An important bridge towards the study of 2D non-separable atom-surface potentials are propagation tests on non-separable potentials. However, the Schrödinger equations cannot, in most cases, be solved analytically for such cases. Since no analytic solutions of 2D non-separable potentials are currently known to the author, an alternative approach was chosen.
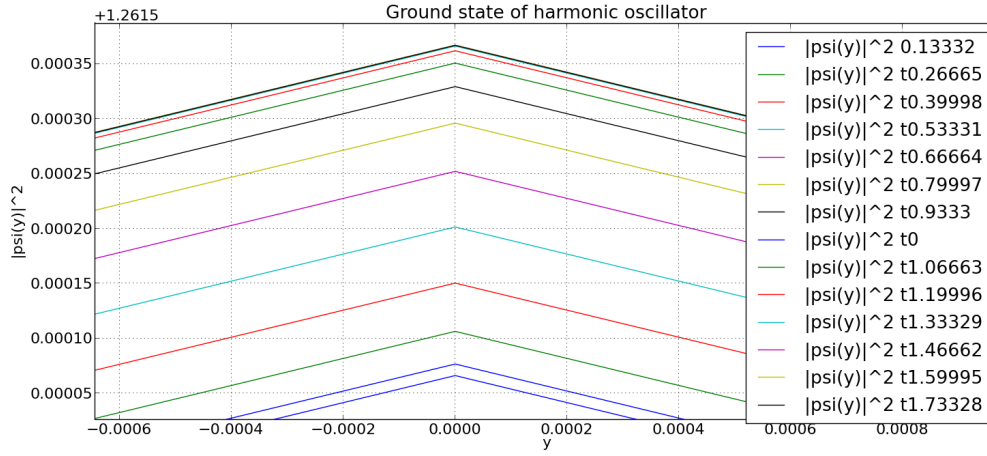
Fig. 3.2 The graph shows a zoom of the maximum of the oscillator ground state at different times. The numerically obtained eigenstate has errors due to finite size approximations, which result in the state to oscillate about its exact form. The frequency of oscillation is given by the period of the oscillator $T = \frac{2\pi}{\omega}$. The relative error at the peak can be read from the graph to be of order 10^{-4}. This error size is comparable to typical error sizes in the 1D studies performed by Herwerth [28].

The key feature of non-separable potentials is the fact that the dynamics along the two dimensions cannot be dealt with along each dimension separately, since momentum transfers can occur between the two dimensions. As a result, the choice of gridpoints along the two dimensions must be sufficient to resolve such dynamics along both numerical axes. In jargon, the two coordinates are coupled.

In order to perform a realistic simulation of this problem without losing the possibility of performing analytic checks of the dynamics of the particle, a tilted oscillator was initially considered.

By considering a one-dimensional harmonic oscillator, whose axis is tilted by an angle ϕ with respect to the x-axis, the Hamiltonian in the x and y coordinates becomes:

$$
\begin{aligned}
H(x,y) &= -\frac{\hbar^2}{2m}\left(\frac{\partial^2}{\partial x'^2} + \frac{\partial^2}{\partial y'^2}\right) + \frac{1}{2}m\omega^2 x'^2 \\
&= -\frac{\hbar^2}{2m}\left(\frac{\partial^2}{\partial x^2} + \frac{\partial^2}{\partial y^2}\right) + \frac{1}{2}m\omega^2(x\cos(\phi) + y\sin(\phi))^2 \\
&= -\frac{\hbar^2}{2m}\left(\frac{\partial^2}{\partial x^2} + \frac{\partial^2}{\partial y^2}\right) + \frac{1}{2}m\omega^2[x^2\cos^2(\phi) + y^2\sin^2(\phi) + 2xy\sin(\phi)\cos(\phi)]
\end{aligned}
\tag{3.6}
$$

where x' is the position along the tilted x-axis, and the invariance of the ∇^2 operator under rotation is used to transform the second derivatives to the new coordinate system [45].

Whilst this system can be solved analytically by means of a change of coordinates, in the frame of reference which our code works with the two variables are coupled, therefore it can effectively be used as a non-separable test of our methods.

The same oscillatory effect as in the separable case was observed along the tilted x axis, although computational costs are higher in this case, since a denser sampling of the grid is necessary in both dimensions (which is very unconvenient along y, as explained in Sec. 2).

In addition to this analytically testable case, the convergence of results obtained for 2D numerical propagation across different potential shapes, such as potential hills of gaussian shape was checked, and the physical behaviour was qualitatively examined.

3.2   QR in 2D for a flat surface

The final test for the 2D code developed in this project has been the comparison of the results for a flat surface with the previous 1D studies. In fact, 1D results can be matched by propagating a 2D gaussian wavepacket across the Casimir-Van der Waals potential for a flat surface (Eq. 4.6) shown in Fig. 4.2. The reflection coefficient for the 1D case is thus recovered by integrating the wavefunction in momentum space with respect to all momentum components along the y direction, as shown in Eq.(1.11). Similarly, the column density can be integrated with respect to y in order to compare the results in real space. Clearly, in order to achieve the best resolution of the potential landscape, the computationally less expensive x (numerical, see Sec.2) axis is used to sample the potential, while the particle is left free to propagate in the y direction.

A separable gaussian wavepacket with initial mean velocity $\mathbf{v} = (-2,0)ms^{-1}$ and spatial spreads $\sigma_x = 0.08\mu m$ and $\sigma_y = 0.01\mu m$ in the x and y directions respectively was propagated across a spatial domain $-1.5\mu m < x < 5.5\mu m$, $-0.1\mu m < y < 0.1\mu m$, where the potential $V(x,y) = V(x)$ is given by Eq.(1.13). Periodic boundary conditions were applied along y. The time range of the simulations was $3.5\mu s$.

As explained in the previous chapter, the computational costs treat the two dimensions very asymmetrically. Hence particular care is needed in choosing the appropriate number of gridpoints along y. Therefore, in order to minimise the computational costs of these tests, the dependence of the reflection coefficient on the number of gridpoints in the second dimension was initially investigated for a continuation distance $x_0 = 10^{-8}$ m.

The result of such tests is shown in Table 3.1. Evidently, the number of gridpoints along y only influences the propagation very marginally. Therefore, it was kept at a convenient value[1] $N_y = 2^4$.

---

[1]However, this choice is only viable under the following three conditions (see next page):

N_y	N_x	R_{2D}	R_{1D}	R_{TI}
2^4	2^{13}	0.015513614	0.01551361	
2^5	2^{13}	0.015513612	0.01551361	
2^6	2^{13}	0.015513251	0.01551361	
2^4	2^{14}	0.015499456	0.015499451	0.01538918
2^5	2^{14}	0.015499453	0.015499451	0.01538918
2^6	2^{14}	0.015499452	0.015499451	0.01538918
2^4	2^{15}	0.0154958	0.0154958	
2^5	2^{15}	0.01549581	0.0154958	
2^6	2^{15}	0.0154957	0.0154958	
-	2^{18}			0.01538917

Table 3.1 The table shows the values obtained for the reflectivity in the time-dependent 2D and 1D cases, as well as with the time-independent approach. The negligible dependence of R on N_y in evident. In this case, the timestep chosen was $\delta t = 10^{-9}s$, and the continuation point chosen was $x_0 = 10$ *nm*.

This result shows that no unwanted couplings occur between the two dimensions, if not as a consequence of an unseparable potential.

As well as the independence of the results of N_y, Table 3.1 gives an accurate comparison between the values for R with the *2D* and *1D* time-dependent methods, as well the corresponding value obtained with the time-independent approach. The quality of the matching between 2D and 1D results remarkable, and the relative deviation from 1D results was found to be, in all cases smaller than 10^{-6}.

The 2D results for the reflectivity are compared to the time-independent curve for different values of the continuation potential in Figs. 3.3. It can be seen that the order of the errors is equivalent to the results for the 1D case obtained in [28] as expected.

Interestingly, a temporary overshoot of the reflectivity was observed, as shown in Fig. 3.4. In our preliminary studies, it was observed that artificial reflections of the absolute order of 10^{-4} are caused by the filter, which is in agreement with the results observed. These spurious reflections cannot be observed from the graphs in cases where the value of the reflectivity is

---

1. The potential does not couple between the two dimensions, so that no momentum is transferred from the *x* to the *y* dimension.

2. The potential is (at least to a good approximation) flat along *y*.

3. Periodic boundary conditions are used. In fact, if reflecting boundaries are used, the wavepacket undergoes fast oscillations as it hits the edge of the numerical box. Such oscillations cannot be effectively resolved which so few gridpoints.
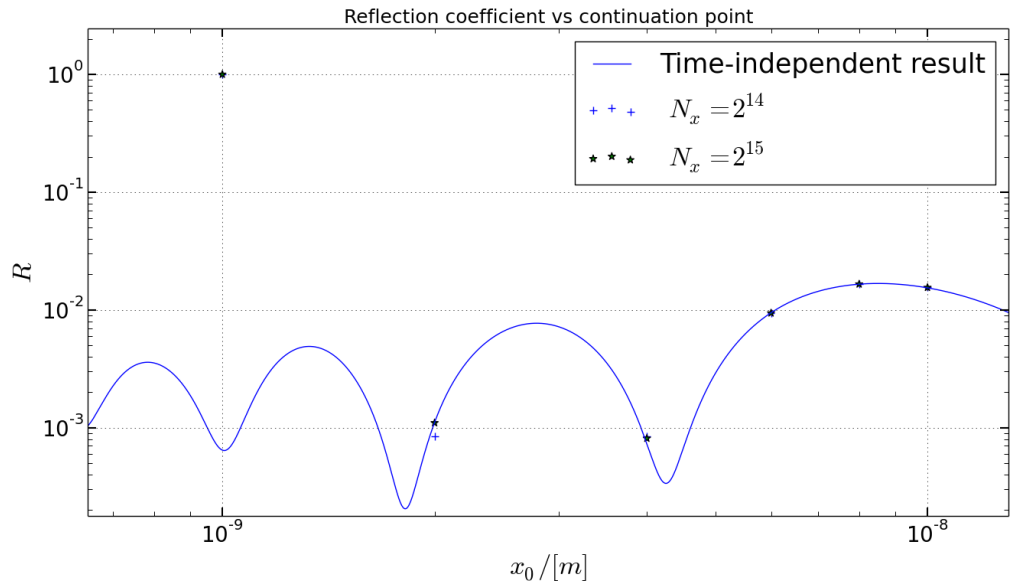
(a)
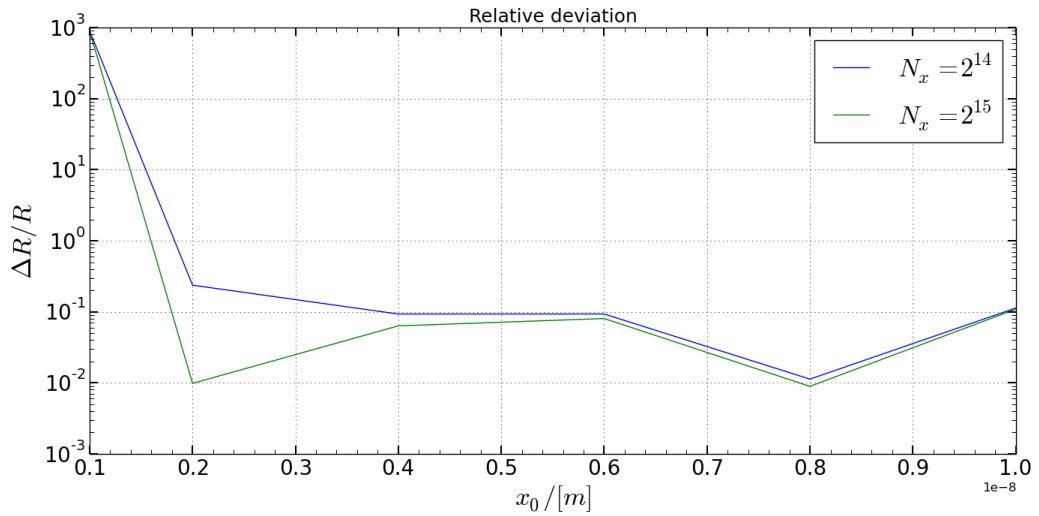
(b)

Fig. 3.3 The graphs shows the results for the reflectivity as a function of the continuation point x_0 obtained by means of the new 2D code with 2^{14} and 2^{15} gridpoints along the x axis. In (a) the 2D time-dependent results are plotted, as well as the time independent curve. From (b) it can be seen that, with both numbers of gridpoints, the results correspond to the time-independent reflection coefficient within a relative error of $\sim 10^{-1}$ for values of the continuation point larger or equal to 4×10^{-9} m. However, the results obtained with 2^{14} gridpoints become unprecise for $x_0 \sim 2 \times 10^{-9}$ m, and both diverge to ≈ 1 for $x_0 = 10^{-9}$ m.

larger than 10^{-3}. However, the deviation shown in Table 3.1 between time-dependent and time-independent results can be explained by these artificial reflections (see Appendix A).
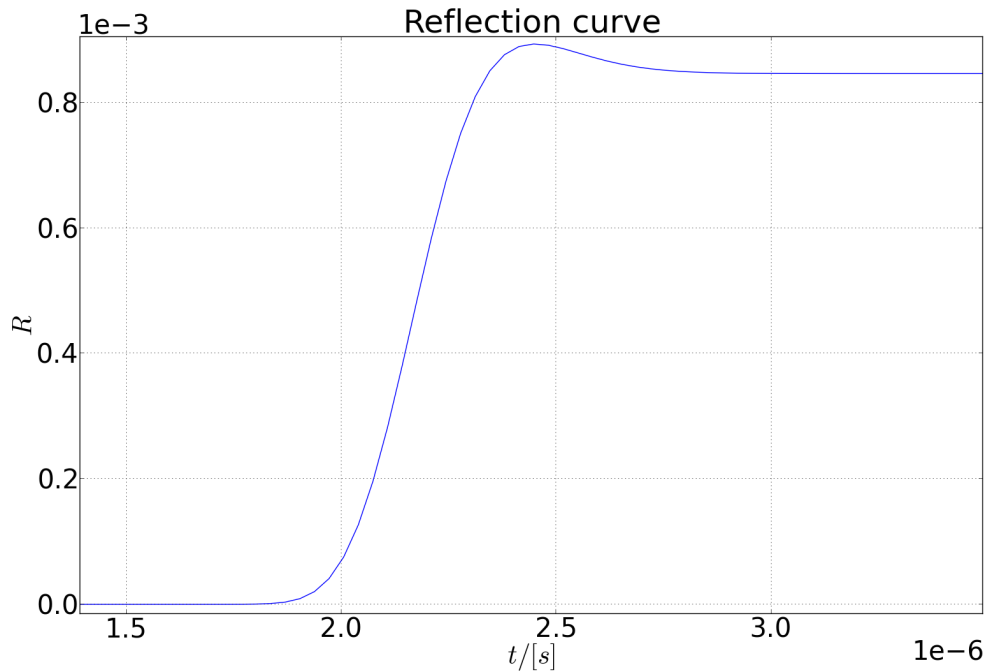
Fig. 3.4 The graph shows the reflection curve obtained with 2^{15} gridpoints along x for a continuation point $x_0 = 2nm$. It can be clearly seen that R overshoots its asymptotic value at $t \approx 2.5\ \mu m$. This is caused by artificial reflections which take place at the filter. However, since the filter then keeps absorbing these artificially reflected components, their effect is partially suppressed. Nevertheless, this effect places a limit (i.e. $\approx 10^{-3}$) to the values of the reflectivity which can be resolved effectively.

Chapter 4

Towards Quantum Reflection off true 2D Surfaces

An important aim of this project will be to study how a periodic corrugation in the attractive surface influences its reflectivity for atoms. Since the exact form of the Casimir-Polder potential has never been calculated for such geometry, an effective generalised potential is proposed for the Casimir-Van der Waals (short-range) regime, which makes use of the Hamaker approximation (see Sec.4.1) [6]. On physical grounds, the potential is required to exhibit the following properties:

1. Its x and y dependencies should not decouple.

2. It should have a periodicity as a result of periodic corrugations in the surface of interaction.

Such generalised potential will later be used to obtain the first results for QR off a periodically corrugated surface.

The continuation of the potential is still required in order to avoid singularities in the potential at positions too close to the surface. To this end, a number of alternative continuation methods to the former 1D approaches [28] are proposed.

4.1 Effective 2D potentials

So far a 1D potential of the form $V(x) \sim x^{-3}$ has been considered, where x is the normal distance to the surface. Such potential already takes into account the interaction with the entire flat surface, although its validity is limited, as discussed in Sec.(1.1), to the regime in

which the distance to the surface x is much smaller than the reduced wavelength of the atomic transition λ (whose value for ^{3}He is ≈ 9.3 *nm*), so that retardation effects are negligible.

Such potential can be derived by means of the Hamaker approximation, which assumes that the interactions between the molecules in the solid and the atom can be treated independently, so that the complete potential can be computed as a sum. Within this regime, the interaction between the atom A and a given molecule B in the solid is governed by the attractive London-Van der Waals potential [6, 27]:

$$V_{AB} = -\frac{C_{AB}}{r^6} \tag{4.1}$$

where:

$$r(\mathbf{P}, \mathbf{S}) = [(x - x_s)^2 + (y - y_s)^2 + (z - z_s)^2]^{1/2} \tag{4.2}$$

is the distance between the point $P = (x, y, z)$ at which the potential is calculated and an arbitrary point $\mathbf{S} = (x_s, y_s, z_s)$ in the solid [6]. C_{AB} is a constant which describes the strength of a single interaction.

Let us consider the following three-dimensional setup: an atom is initially located at a certain point $P = (x, y, z)$, with $x > 0$. A metallic, infinitely thick and wide solid lies below it, with its surface lying on the $y - z$ plane. A graphical representation is given in Fig. 4.1.

In order to add the contributions from all the molecules in the solid, a given molecular density ρ_B is considered, which is assumed to be constant over the solid. Therefore, the sum of all contributions from the molecules in the flat solid can be written:

$$V(x, y, z) = \int_V \rho_B V_{AB} dV \tag{4.3}$$

This integration can be conveniently performed in cylindrical coordinates [6]:

$$x_s = x_s \tag{4.4a}$$

$$y_s = \rho_s \sin(\phi_s) \tag{4.4b}$$

$$z_s = \rho_s \cos(\phi_s) \tag{4.4c}$$

Since the surface is flat, the contributions are independent of the angle ϕ. Moreover, by symmetry, for an infinite surface:

$$V(x, \rho, \phi) = V(x) \tag{4.5}$$
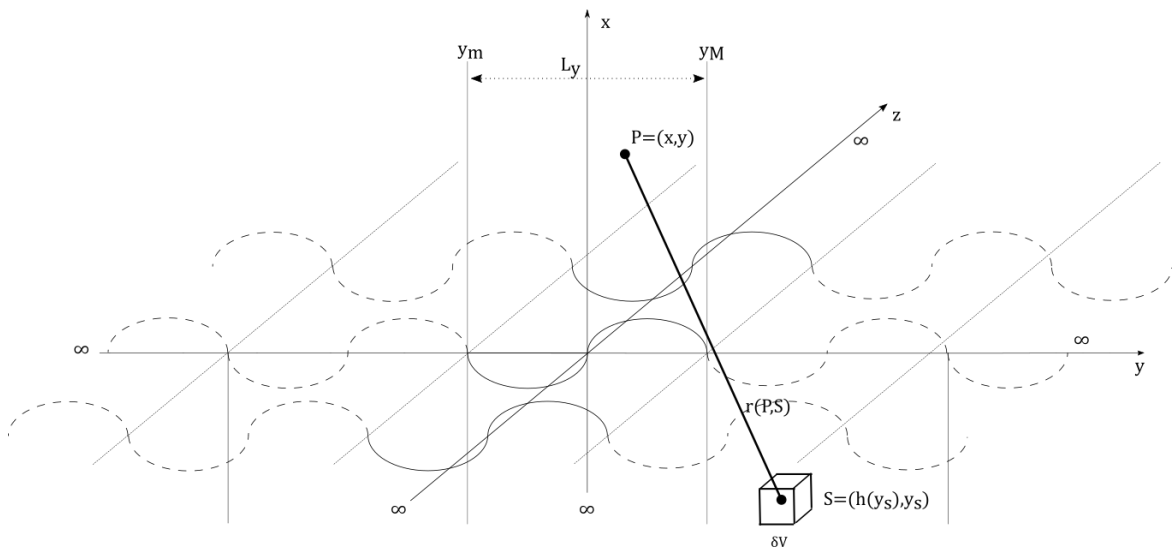
Fig. 4.1 The diagram shows the structure of the corrugated surface over which the single-interaction contributions are summed according to Hamaker theory. The surface is assumed to be infinitely wide ($y \to \pm\infty$), long ($z \to \pm\infty$) and thick (x ranges from $-\infty$ to $h(y)$). In the propagation of the wavepacket, periodic boundary conditions (PBCs) will be applied, so that only a single sinusoidal region needs to be sampled. The continuous vertical lines next to the x axis enclose such region, while the dotted corrugations represent regions which are only accounted for via the PBCs.

Hence the potential due to the interaction with a flat surface is given by:

$$
\begin{aligned}
V(x) &= -2\pi C_{AB}\rho_B \int_{-\infty}^{0} dx_s \int_{0}^{\infty} \rho_s \frac{d\rho_s}{[(x+x_s)^2 + \rho_s^2]^3} \\
&= \frac{\pi}{2} C_{AB}\rho_B \int_{-\infty}^{0} \frac{1}{(x+x_s)^4} dx_s \\
&= -\frac{\pi C_{AB}\rho_B}{6} \frac{1}{x^3}
\end{aligned}
\tag{4.6}
$$

Thus, since the constant C_3 is known experimentally [38], the product of the constants C_{AB} and ρ_B can be determined directly by comparing Eq. (1.3) with Eq. (4.6), so that: $C_{AB}\rho_B = \frac{6C_3}{\pi}$.

This approach was originally proposed by Hamaker in 1937 [27], and is generally known in surface science as Hamaker theory. A more rigorous approach was later taken by Lifschitz [39], who showed that the Hamaker approximation in fact yields the correct results within the regime that was already mentioned [6].

However, the validity of this approach is limited to the non-retarded regime. In fact, retardation effects would weaken the strength of the interaction, as mentioned in Sec. 1.1. More comprehensive treatments of this problem, which would include retardation effects, are studied in depth using quantum field theory approaches . In particular, studies of periodic surfaces were performed by Döbrich et al. [17] and Droujina et al. [18].

In order to generalise Eq.(4.6) to an arbitrary surface, the limits of integration in x are modified as follows:

$$
V(x,y,z) = -\frac{6C_3}{\pi} \int_{-\infty}^{+\infty} dz_s \int_{-\infty}^{+\infty} dy_s \int_{-\infty}^{h(y_s)} \frac{1}{r(x_s,y_s,z_s)^6} dx_s
\tag{4.7}
$$

where $h(y_s)$ denotes the height of the surface corrugation. The condition $h(y_s) < x$ needs to be imposed in order to avoid the singularity at $r \to 0$, where a smooth continuation will replace the potential.

The system is assumed to be symmetric along the z axis. Moreover, the surface is assumed to be periodic along y. Namely, it satisfies the condition: $h(y) = h(y + nL_y)$, where L_y is the period of such structure and $n \in \mathbb{Z}$.

Due to the periodic structure of the surface, $h(y_s)$ can thus be generally written as a Fourier series. Therefore, as an approximation, a sinusoidal shape is assumed for the surface

height. Hence, the shape of the surface can be expected to be approximately described by the function:

$$h(y_s) = A[1 + \sin(\omega y_s + \phi)] \tag{4.8}$$

where y_s is the position along the surface, A is the amplitude of such sinusoidal corrugation, ω its spatial angular frequency, and ϕ an arbitrary phase shift. Eq.(4.8) corresponds to the height of an additional sinusoidal corrugation which enters the region of space where $x > 0$. This surface function could be generalised to an arbitrary periodic shape by adding higher order Fourier components.

Eq.(4.7) can be evaluated numerically. However, in order to determine the existence of such integral, the positivity of the integral is initially considered. Consider the potential described by Eq.(4.6) for a flat surface at $x = 0$. The same result can be applied to a case in which an additional flat slab of width $2A$, where $A \in (0, x/2)$ is added to the surface of the solid.

Since the distance between the point $\mathbf{P}$ and the surface is thus reduced by $2A$, our analytical formula would yield the value:

$$\tilde{V} = -\frac{C_3}{(x - 2A)^3} \tag{4.9}$$

Clearly, the following relation holds:

$$|\tilde{V}(A)| > |V| \quad \forall A \in (0, x/2) \tag{4.10}$$

Given a region R in an euclidean space, which can be divided into two regions R_A and R_B such that $R = R_A + R_B$, and assuming that $f(\mathbf{r})$ is a real, continuous and differentiable function over the region R, the following identity holds [33]:

$$\int_R f(\mathbf{r}) dV = \int_{R_A} f(\mathbf{r}) dV + \int_{R_B} f(\mathbf{r}) dV \tag{4.11}$$

Hence, the difference between the two cases must be given by:

$$\Delta V = \tilde{V} - V = -C_3 \left(\frac{1}{(x - 2A)^3} - \frac{1}{x^3} \right) \tag{4.12}$$

Now consider the case in which such slab is not flat, but its height depends on y, such that each additional volume element belongs to the interval $0 \leq x_s \leq A(1 + \sin(\omega y_s))$:

Since the integrand is always positive, the contribution from the additional sinusoidal slab must be given by:

$$\Delta V_{corr} = -\frac{6C_3}{\pi} \int_{-\infty}^{+\infty} dz_s \int_{-\infty}^{+\infty} dy_s \int_0^{A[1+\sin(\omega y_s)]} \frac{1}{r(x_s,y_s,z_s)^6} dx_s < \Delta V \tag{4.13}$$

Thus, an upper bound is obtained for the additional contribution to the potential from a sinusoidal slab, which can be simply added to the analytical result, thus avoiding part of the numerical effort in the computation of the integral. Therefore, the complete potential for a corrugated surface can finally be written as:

$$V_{corr} = V(x) - \frac{6C_3}{\pi} \int_{-\infty}^{+\infty} dz_s \int_{-\infty}^{+\infty} dy_s \int_0^{A[1+\sin(\omega y_s)]} \frac{1}{r(x_s,y_s,z_s)^6} dx_s \tag{4.14}$$

4.2   2D continuation of the potential and filtering

The integrand in Eq.(4.14) becomes singular as $r(x_s,y_s,z_s) \to 0$. This occurs for points which lie on the surface, namely when $x = h(y_s)$. Therefore, similarly to the 1D approach, a continuation distance d_c from the surface is defined, over which the potential is smoothly continued along x, in order to make the potential converge to a constant value beyond the surface, where the wave will be numerically filtered in order to eliminate artificial reflections at the negative x-edge of the grid.

At the present stage, a 1D filter is used along x only, i.e. the filtering function acts homogeneously for all y by generalising the sigmoidal filter designed by Herwerth [28]. This is the most obvious initial choice, since the extent of the asymmetry of the wavepacket along y resulting from couplings of the corrugated surface potential are not known. A number of alternative filters are discussed in the outlook.

The overall structure of the potential is divided, for each point in y, in three regions:

1. Propagation region: it corresponds to positions above the surface, at a distance such that the depth and slope of the potential can be handled numerically.

2. Continuation region: beyond a certain value $x > d_c$, which can be defined by three different criteria (see below), the potential is continued as a polynomial, whose coefficients will depend smoothly on y. Such polynomial smoothly brings the value of the potential to a constant value for each y.

3. Plateau region: this is the portion of our spatial domain beyond the surface. Here the potential is constant along x, and the numerical filter is applied.

Such a continuation method would avoid any momentum transfers between the two dimensions, thus allowing a better manipulation of the component of the wavepacket which has to be suppressed.

It might be preferable, if not necessary, to design the continuation region of the potential such that both the x and y dependence of the potential are suppressed, thus reaching a constant value V_0 at $x = h(y)$, namely where the distance to the surface along x is 0.

Firstly a continuation condition has to be chosen, which will define the curve $f(x,y) = 0$ along which the potential will be continued.

To this end, three approaches have been considered:

1. A threshold constant vertical (i.e. along x) distance $\Delta x_c = x_c(y) - h(y)$ to the surface exactly beneath the point $\mathbf{P} = (x, y)$, at which the potential is calculated, (i.e. at the same y position) is defined. The potential is thus continued for values of $x(y) - h(y) < \Delta x_c$. This approach has been chosen in 1D studies [29]. It is the easiest continuation criterion to implement, and it was applied to the case of a flat surface for which it yield equivalent results to the 1D studies performed by Sünderhauf and Herwerth [50] [29]. However, as the extent of the surface corrugation becomes comparable to its period, the contributions to the integral (4.7) from the finite elements of the surface for which $A\sin(\omega y) \simeq x$ and $y_s \simeq y$) will become too large. In order to avoid this behaviour, the condition $\Delta x_c > A$ must be fulfilled, which would, however, prevent the possibility of computing the potential between peaks of the corrugated surface.

2. The problem which would arise as a result of the corrugation has been overcome by generalising the vertical threshold distance to the distance between $\mathbf{P}(\mathbf{x}, \mathbf{y})$ and the closest point of the surface. This can be performed by minimising the distance:

$$r(x, x_s, y, y_s) = \sqrt{(x - A\sin(\omega y_s))^2 + (y - y_s)^2} \qquad (4.15)$$

between $\mathbf{P}$ and the surface with respect to y_s.

Since the closest distance to a flat surface corresponds to its normal distance (i.e. in this case along x), this approach trivially reduces to the first method in the case of a flat surface. This new method was implemented and tested. The minimisation of the function (4.15) is performed by means of a golden section search algorithm [43] only for points which are close enough to a minimum vertical threshold distance to the surface, in order to avoid unnecessary computation.

3. A threshold constant value of the potential is defined, which defines a curve $f(x, y)$. Thus, for values of d_c smaller than the corresponding threshold, the potential is

continued. This approach has the advantage of keeping control of the relevant physical quantity, namely the potential energy, so that any singularities are directly excluded. However, this approach was not adopted in previous treatments of this problem, hence it cannot be directly mapped to one-dimensional results. Hence, although the method was tested by plotting the potential, its effectiveness has not yet been compared with the distance-based continuation criteria.

It can be seen, however, that the difference between the three approaches vanishes as the amplitude of the corrugation tends to zero.

4.2.1   Continuation functions for the potential

Once a criterion for continuation is chosen, the constraints on the continuation function V_c have to be determined. In order to smoothly bring the potential to a constant value both in x and y, we seek a continuous and differentiable function which allows at least the following three conditions to be simultaneously satisfied for any value of y:

- $V(d_c) = V_c(d_c)$

- $\frac{\partial V(d_c)}{\partial x} = \frac{\partial V_c(d_c)}{\partial x}$

- $\frac{\partial V_c(0)}{\partial x} = 0$

Note that the values of the potential are generally not known analytically, but rather stored in a vector. Numerical derivatives can generally computed numerically as:

$$\left.\frac{\partial V}{\partial x}\right|_{x_i} \simeq \frac{V(x_{i+1}) - V(x_{i-1})}{2\delta x} \tag{4.16}$$

This can be easily proven by Taylor expansion [43].

However, since the region where the differentiation is performed is in proximity of a singularity, such function varies rapidly along x, hence a slightly more sophisticated, 8th order accurate version was implemented [20]. The consequent increase in computational costs is negligible, since such operation is only performed n_y times over the whole simulation.

If no further constraints are imposed on the continuation function, a parabolic continuation can be used as in the 1D studies performed by Herwerth and Sünderhauf [29][50]. While this method has been heavily tested by Herwerth [28], for a corrugated surface it has the drawback that the potential is not constant along y for $x < 0$. This might cause problems with the filtering of the wavepacket since scattering processes will occur along y as a result

of the remaining corrugation of the potential. Further research is needed in order to verify this effect.

In order to avoid this effect, however, an alternative method was also implemented. By choosing a third degree polynomial, an additional constraint can be imposed on V_c, namely:

$$V_c(0) = V_0 \tag{4.17}$$

This is equivalent to fixing a constant value V_0 is fixed, at which the potential must converge for all y. The value of V_0 has to be fixed arbitrarily by considering that:

- A value of V_0 which is too low (i.e. too large in absolute value) might cause spurious reflections or even a breakdown of the numerical scheme due to the excessive steepness of the continuation function.

- On the other hand, V_0 must be kept smaller than $V(x_c(y)) \; \forall y$, otherwise a minimum of the potential will form at the continuation point, which would generate unwanted scattering effects.

Clearly, the difficulties associated with the simultaneous fulfillment of such constraints increase with the amplitude of the corrugation, since the same value of V_0 must be plausible for all values of y, whose respective values of $V(x_c(y))$ can become significantly different.

The form of the continuing function would then be:

$$V_c(x,y) = \alpha(y)(x - h(y))^3 + \beta(y)(x - h(y))^2 + \gamma(y)(x - h(y)) + \delta \tag{4.18}$$

whose four coefficients depend on y, and ensure the the conditions above are fulfilled. One can immediately notice that $\delta = V_0$ in order to satisfy $V_c(h(y), y) = V_0$ as required above, and by matching the other three boundary conditions the other three parameters are determined. It is important to note that $V_c(x,y)$ needs to behave differently at different values of y in order to match the local potential values, hence three of such parameters need a y dependence. However, the functional shape for a fixed y is a cubic function.

By solving the system above the four parameters are:

$$\alpha(y) = \frac{1}{(x_c - h(y))^2} \left[\frac{2V_0(y)}{x_c - h(y)} + \frac{\partial V}{\partial x}\bigg|_{x=x_c} - \frac{2V_c(y)}{x_c - h(y)} \right] \tag{4.19a}$$

$$\beta(y) = \frac{1}{x_c - h(y)} \left[\frac{3V_c(y)}{x_c - h(y)} - \frac{\partial V}{\partial x}\bigg|_{x=x_c} - \frac{3V_0(y)}{x_c - h(y)} \right] \tag{4.19b}$$

$$\gamma(y) = 0 \tag{4.19c}$$
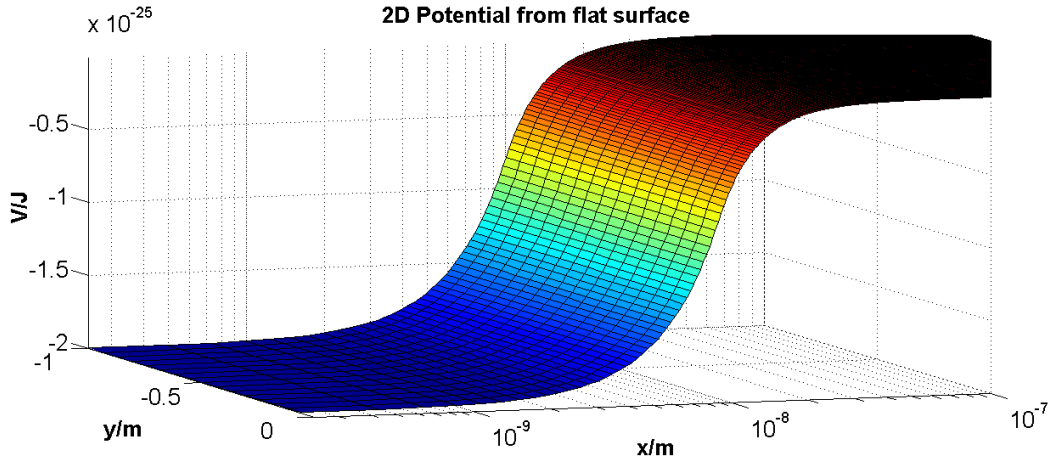
Fig. 4.2 The 3D plot shows the 2D potential in the flat surface case with a cubic continuation. The x-axis is in logarithmic scale, hence only the values for $x > 0$ can be represented in this plot. However, the convergence of the potential to a constant value as $x \to 0^+$ is evident.

$$\delta = V_0 \tag{4.19d}$$

The main disadvantage of this method is the steeper shape of the cubic function in comparison to a parabola, which needs careful optimisation. In fact, our preliminary numerical tests showed a relative increase in the reflectivity of order 10^{-2} in the case of a cubic continuation compared to the parabolic case. Therefore, the parabolic continuation was preferred in order to reproduce 1D results for a flat surface (Sec. 3.2).

The potential for a flat surface with a cubic continuation is shown in Fig. 4.2. The shape of the potential is qualitatively equivalent to the case of a parabolic continuation, although slight differences in the continuation region, which is where QR is most sensitive to the shape of the potential, resulted in a slight systematic increase in the reflectivity of relative order 10^{-1}.
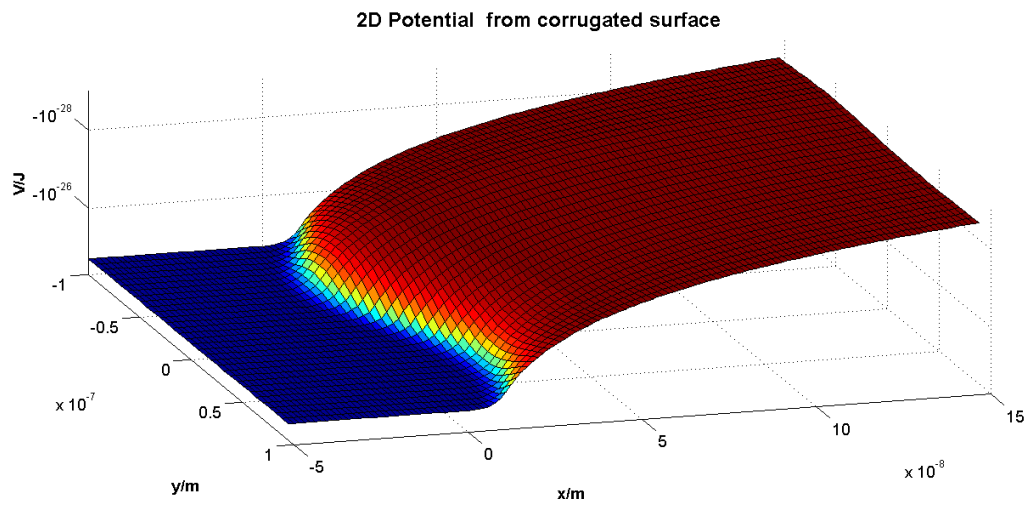
Fig. 4.3 The graph shows the behaviour of the effective potential which results from the interaction with an attractive corrugated surface. As expected, the position at which the potential drops follows the shape of the corrugation. The z axis (potential energy) is in logarithmic scale. The amplitude A chosen for the surface corrugation is $10nm$, while its length period L is $200nm$. The cubic continuation was applied at a fixed distance $d_c = x_c - A = 10nm$ from the surface.
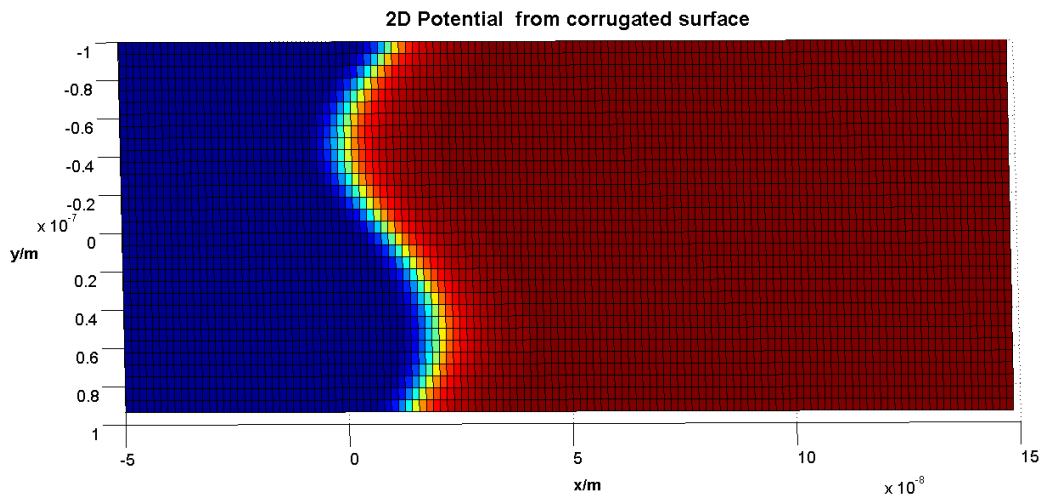
Fig. 4.4 The graph shows a vertical view of the 2D potential for a corrugated surface shown in Fig. 4.3. From this plot the amplitude of the corrugation in the potential can be easily compared to the size of the corrugation. It can be seen that such amplitude is approximately 10 nm, which matches the amplitude of the corrugation.

Chapter 5

Conclusions

In this project, a numerical algorithm was implemented and tested, which will enable the first studies of QR off 2D non-separable potential structures in the time domain.

The method developed was found to be particularly suitable for problems where the scattering potential is periodic along one of the two dimensions, due to the highly asymmetric dependence of computational costs on the number of gridpoints along the two dimensions.

In order to achieve an understanding of the physical problem to model, preliminary studies of 1D systems were performed by using existing codes [28, 50]. In fact, 1D codes are an essential tool in the transition to the 2D treatment, since they can be used to test for accuracy in limiting cases and more generally to investigate the dynamics of the wavepacket in simplified regimes. In particular, the fact that the potential step is an upper bound to the reflectivity allows reliable checks of the numerical results for more complicated potential structures. Furthermore, the occurrence of spurious reflections at the filter was detected in this context.

Thus, propagation tests were carried out on well known systems for which analytical solutions are available. Firstly, the 2D free propagation of a gaussian wavepacket was performed numerically and the evolution of its spatial spread was compared to the analytic result. The dynamics of a free particle could be modelled very accurately via our numerical procedure even with a small number of gridpoints. However, this result does not have any remarkable importance in the modeling of the problem, since no potential landscape is present, and it is only to be regarded as a routine test. Nevertheless, the effective reliability of the results for smaller numbers of gridpoints allowed an optimisation of the computational costs in other tests.

The ground state of a 1D harmonic oscillator was tested in 2D and its stationary behaviour checked. Oscillations of the maximum value of the ground state around the exact peak were observed at the characteristic frequency of the oscillator by calculating the column density

function along the dimension of interest. These oscillations are finite size effects which can be reduced by increasing the number of gridpoints. The fact that they occur at the characteristic frequency of the oscillator denotes that the physical properties of the system are accurately described by the numerical algorithm. Moreover, their relative size was observed to be of order 10^{-4}. This is consistent with the characteristic size of the errors which are typically obtained with this method [54]. The dynamics of the oscillator was observed as well by propagating a slightly displaced state into the oscillator, and the expected frequency of oscillation was observed. Furthermore, the same can be concluded for the propagation of the ground state of a tilted harmonic oscillator. This was performed in order to investigate propagation in a potential which effectively couples the two dimensions in the coordinate system which the numerical scheme works with.

The results for a flat surface originally obtained in 1D by Herwerth [28] were reproduced by integrating the contributions to R along the second dimension. The matching of these results is remarkably precise, and the largest relative deviations measured were of the order of 10^{-5}. This result is regarded, together with the preliminary propagation tests, as the key evidence that our methods can be effectively applied to the problem of QR in two dimensions. However, the fact that relative errors in the reflection coefficient obtained via time-dependent schemes were never found (within non-flat potential structures) to be smaller than 10^{-4} leads us to the conclusion that, with typical numbers of gridpoints used, this is the best precision which can be achieved by our method.

In order to enable the first tests of QR off a corrugated surface, a generalisation of the $1/x^3$ potential was developed in the framework of the classical Hamaker approximation, and the methods used to continue the potential in proximity of the singularity were generalised in order to be applied to fully two dimensional potentials.

Since the central aim of this work is to provide a proof of concept of the applicability of our methods to the study of QR, significant improvements are believed to be possible in future developments of the project.

5.1 Outlook

Although the implementation of an efficient time-dependent algorithm for the numerical study of QR was successful, further investigations are necessary in order to optimize the numerical procedures and evaluate their capabilities in a diverse range of applications. The next task to be performed a clearly is clearly the first test of QR with the new corrugated potential. This will enable several further improvements of our numerical methods.

To begin with, an accurate tuning of the spatial and temporal step sizes for the non-separable atom-surface potential needs to be performed, and a profile of the correlations between the spatial and temporal steps for such case has to be traced.

A detailed profiling of the code needs to be carried out, in order to investigate alternative, more efficient options in the implementation of the numerical routines. Moreover, further options might be explored by considering details of the optimisers offered by different compilers, and eventually adjusting the routines accordingly.

Although the five point approximation was considered to be ineffective along the x axis[1], the asymmetric nature of the method makes the additional costs associated to the use of the five-point approximation along y only marginally higher[2]. This might help to reduce the number of gridpoints which are necessary in order to resolve the oscillations which would arise along y in a strongly non-separable regime, i.e. when the amplitude of the corrugation in the surface becomes comparable to the period of the sinusoid.

Another future aim of this project are numerical tests for diffraction effects as a result of reflection off periodic structures. This effect has been recently investigated theoretically by Stickler et al. [49], who considered QR off a periodically doped surface. In order to obtain this effect, three length scales should be matched: the De Broglie wavelength of the incoming particle perpendicular to the surface should match the wavelength of the periodic surface in order for constructive interference to occur. However, the distance to the surface must match the potential regime where QR occurs. A first step in the numerical study of this problem has been made by Herwerth et al. [29], who studied QR in 1D off an oscillating potential. In the regime where the particle approaches the periodic surface at grazing incidence, the 2D problem could, in principle, be mapped onto a 1D time-dependent problem via a number of approximations in the form of the potential. This possibility, however, is still an open question, and further theoretical investigations are necessary in order to formulate the problem rigorously.

In the near future, further efforts will be put in the search for an analytical expression for the potential of interaction with a corrugated surface (Eq. (4.14)). This will provide a better insight in the expected 2D scattering dynamics of the wavepacket, which is essential for an appropriate tuning of the physical and numerical parameters.

Once the first tests of the wavepacket dynamics in a non-separable potential will be carried out, further investigations will be necessary in order to evaluate the suitability of the current 1D filter with such potentials. This may lead to the design of a new numerical filter.

---

[1]This is due to the fact that the size of the $\mathscr{L}$ matrix would increase by a factor of 2 without significant improvements in the results [28].

[2]This is due to the fact that the additional elements required by the five-point approximation along y would be inside the band of the Hamiltonian matrix.

A possibility in this direction could be a self-tuning filter, which automatically adapts its shape depending on the properties of the incoming wave. In 2D this is a complicated task, since it cannot yet be invesigated analytically, but requires a comprehensive numerical study of the response of the wavepacket to the filter.

Furthermore, the methods which were developed in this project for the study of quantum reflection would easily find a wide range of application in problems which require the numerical propagation of quantum wavepackets in the cases where the potential cannot be solved analytically. For instance, the possibility of applying our methods to disordered potentials with a given correlation length has been considered. Finally, further applications of this 2D treatment could be found in scattering problems on single-layer structures such as graphene.

Finally, since the runtime for $\mathscr{L}\mathscr{L}^t$ decomposition grows as a cubic function with n_y, computational costs could be reduced significantly in cases where n_y can be kept relatively small ($\leq 2^7$). This would allow for the study of 2D time-dependent potentials, whose increase in computational costs would consist entirely of the additional runtime needed to perform $\mathscr{L}\mathscr{L}^t$ decomposition at each timestep, or alternatively, at more widely spaced timesteps.

In the realm of this thesis, significant progress was made towards the achievement of 2D numerical simulations of QR in the time domain. Nevertheless, our work has only begun to open a range of new opportunities in the study of QR, and further efforts will allow our present achievements to find applications across several areas of physics.

References

[1] Ajaib, M. A. (2013). Numerical methods and causality in physics. *arXiv preprint arXiv:1302.5601*.

[2] Andrews, D. and Romero, L. D. (2001). Conceptualization of the Casimir effect. *European Journal of Physics*, 22(4):447.

[3] Babb, J. F. (2005). Long-range atom-surface interactions for cold atoms. In *Journal of Physics: Conference Series*, volume 19, page 1. IOP Publishing.

[4] Bhushan, B. (2013). *Principles and applications of tribology*. John Wiley & Sons.

[5] Bretscher, E. and Cockcroft, J. (1955). Enrico Fermi. 1901-1954. *Biographical Memoirs of Fellows of the Royal Society*, 1:69–78.

[6] Butt, H.-J. and Kappl, M. (2009). *Surface and interfacial forces*. John Wiley & Sons.

[7] C. Cohen-Tannoudji, B. D. and Laloe, F. (1977). *Quantum Mechanics*, volume 1.

[8] Capasso, F., Munday, J. N., Iannuzzi, D., and Chan, H. (2007). Casimir forces and quantum electrodynamical torques: Physics and nanomechanics. *Selected Topics in Quantum Electronics, IEEE Journal of*, 13(2):400–414.

[9] Casimir, H. B. (1948). On the attraction between two perfectly conducting plates. In *Proc. K. Ned. Akad. Wet*, volume 51, page 150.

[10] Crank, J. and Nicolson, P. (1947). A practical method for numerical evaluation of solutions of partial differential equations of the heat-conduction type. In *Mathematical Proceedings of the Cambridge Philosophical Society*, volume 43, pages 50–67. Cambridge Univ Press.

[11] Dalvit, D., Lombardo, F., Mazzitelli, F., and Onofrio, R. (2006). Exact Casimir interaction between eccentric cylinders. *Physical Review A*, 74(2):020101.

[12] DeKieviet, M. (2015). Private communication on current experimental data.

[13] DeKieviet, M., Dubbers, D., Hafner, S., and Lang, F. (2001). Atomic beam spin echo. principle and surface science application. In *Atomic and Molecular Beams*, pages 161–174. Springer.

[14] DeKieviet, M., Dubbers, D., Klein, M., Pieles, U., and Schmidt, C. (2000). Design and performance of a highly efficient mass spectrometer for molecular beams. *Review of Scientific Instruments*, 71(5):2015–2018.

[15] DeKieviet, M., Dubbers, D., Schmidt, C., Scholz, D., and Spinola, U. (1995). 3 he spin echo: New atomic beam technique for probing phenomena in the nev range. *Physical review letters*, 75(10):1919.

[16] DeKieviet, M., Jentschura, U. D., and Łach, G. (2011). Modern experiments on atom-surface casimir physics. In *Casimir Physics*, pages 393–418. Springer.

[17] Döbrich, B., DeKieviet, M., and Gies, H. (2008). Scalar Casimir-Polder forces for uniaxial corrugations. *Physical Review D*, 78(12):125022.

[18] Droujinina, V. (2003). On quantum reflection and the Casimir effect: application to atom-surface scattering.

[19] Dufour, G., Guérout, R., Lambrecht, A., Nesvizhevsky, V., Reynaud, S., and Voronin, A. Y. (2013). Quantum reflection of antihydrogen from nanoporous media. *Physical Review A*, 87(2):022506.

[20] Fornberg, B. (1988). Generation of finite difference formulas on arbitrarily spaced grids. *Mathematics of computation*, 51(184):699–706.

[21] Friedrich, H. and Friedrich, H. (2006). *Theoretical atomic physics*, volume 3. Springer.

[22] Friedrich, H., Jacoby, G., and Meister, C. G. (2002). Quantum reflection by Casimir–Van der Waals potential tails. *Physical Review A*, 65(3):032902.

[23] Galbraith, I., Ching, Y. S., and Abraham, E. (1984). Two-dimensional time-dependent quantum-mechanical scattering event. *American Journal of Physics*, 52(1):60–68.

[24] Garrido, P. L., Goldstein, S., Lukkarinen, J., and Tumulka, R. (2011). Paradoxical reflection in quantum mechanics. *American Journal of Physics*, 79(12):1218–1231.

[25] Goldberg, A., Schey, H. M., and Schwartz, J. L. (1967). Computer-generated motion pictures of one-dimensional quantum-mechanical transmission and reflection phenomena. *American Journal of Physics*, 35(3).

[26] Griffiths, D. J. (2005). *Introduction to Quantum Mechanics*.

[27] Hamaker, H. (1937). The London—Van der Waals attraction between spherical particles. *physica*, 4(10):1058–1072.

[28] Herwerth, B. (2011). Dynamics of quantum reflection in atom-surface interactions. Master's thesis, University of Heidelberg.

[29] Herwerth, B., DeKieviet, M., Madroñero, J., and Wimberger, S. (2013). Quantum reflection from an oscillating surface. *Journal of physics. B. Atomic, molecular and optical physics*, 46(14).

[30] Horn, R. A. and Johnson, C. R. (2012). *Matrix analysis*. Cambridge university press.

[31] Ihm, G., Cole, M. W., Toigo, F., and Scoles, G. (1987). Systematic trends in Van der Waals interactions: Atom–atom and atom–surface cases. *The Journal of chemical physics*, 87(7):3995–3999.

[32] Jaffe, R. (2005). Casimir effect and the quantum vacuum. *Physical Review D*, 72(2):021301.

[33] Jeffreys, H. and Jeffreys, B. (1999). *Methods of mathematical physics*. Cambridge university press.

[34] Jeske, F., Stöferle, T., and DeKieviet, M. (2011). Massive spin-momentum entanglement measured in an atomic beam spin echo experiment. *The European Physical Journal D*, 63(1):25–32.

[35] Klein, A. and Werner, S. (1983). Neutron optics. *Reports on Progress in Physics*, 46(3):259.

[36] Koester, L., Rauch, H., and Seymann, E. (1991). Neutron scattering lengths: a survey of experimental data and methods. *Atomic Data and Nuclear Data Tables*, 49(1):65–120.

[37] Łach, G., DeKieviet, M., and Jentschura, U. D. (2010a). Multipole effects in atom-surface interactions: A theoretical study with an application to he–α-quartz. *Physical Review A*, 81(5):052507.

[38] Łach, G., DeKieviet, M., and Jentschura, U. D. (2010b). Noble gas, alkali and alkaline atoms interacting with a gold surface. *International Journal of Modern Physics A*, 25(11):2337–2344.

[39] Lifshitz, E. (1956). The theory of molecular attractive forces between solids.

[40] Munday, J. N., Capasso, F., and Parsegian, V. A. (2009). Measured long-range repulsive Casimir–Lifshitz forces. *Nature*, 457(7226):170–173.

[41] Parsegian, V. A. (2005). *Van der Waals Forces*. Cambridge University Press. Cambridge Books Online.

[42] Power, E. (2001). Casimir-Polder potential from first principles. *European Journal of Physics*, 22(4):453.

[43] Press, W. H. (2007). *Numerical recipes 3rd edition: The art of scientific computing*. Cambridge university press.

[44] Rae, A. I. M. (2008). *Quantum Mechanics*. Taylor & Francis, fifth edition. p. 43-48.

[45] Riley, K., Hobson, M., and Bence, S. (1999). Mathematical methods for physics and engineering. *American Journal of Physics*, 67(2):165–169.

[46] Rodriguez, A. W., Munday, J., Joannopoulos, J., Capasso, F., Dalvit, D. A., and Johnson, S. G. (2008). Stable suspension and dispersion-induced transitions from repulsive Casimir forces between fluid-separated eccentric cylinders. *Physical review letters*, 101(19):190404.

[47] Shimizu, F. (2001). Specular reflection of very slow metastable neon atoms from a solid surface. *Physical review letters*, 86(6):987.

[48] Squires, G. L. (2012). *Introduction to the theory of thermal neutron scattering*. Cambridge university press.

[49] Stickler, B. A., Even, U., and Hornberger, K. (2015). Quantum reflection and interference of matter waves from periodically doped surfaces. *Physical Review A*, 91(1):013614.

[50] Sünderhauf, C. (2014). Quantum reflection in time and space. Master's thesis, University of Heidelberg, Germany.

[51] Thomas, J. W. (2013). *Numerical partial differential equations: finite difference methods*, volume 22. Springer Science & Business Media.

[52] Vidali, G., Ihm, G., Kim, H.-Y., and Cole, M. W. (1991). Potentials of physical adsorption. *Surface Science Reports*, 12(4):135–181.

[53] Warring, U. (2006). Auf der Suche nach dem perfekten Quantenreflex. Master's thesis, University of Heidelberg. p.16.

[54] Wimberger, S. (2014). Private communication.

Appendix A

Quantum Reflection off a 1D Step Potential

The one-dimensional problem of a quantum particle approaching a one dimensional potential step is well known, and the existence of an analytical solution makes it an ideal workbench to test the methods developed by Herwerth [29] [28] and Sünderhauf [50] for the study of quantum reflection in 1D. From a numerical point of view, the steepness of such potential makes this problem computationally non-trivial. Furthermore, as described in [24], the potential step is the limiting case for which QR is maximised compared to any other functional form for a decrease in the potential. This fact makes it a natural starting point in order to achieve an understanding of QR and a feeling of the response of the numerical scheme to steep potentials.

In this appendix the numerical solutions obtained by means of the time-dependent method presented in Sec. 1.3.1 .

In order to ensure the continuity required by the numerical scheme used, the potential step is approximated by means of a hyperbolic tangent function, whose steepness can be controlled by means of a scaling length parameter a. The convergence of the reflection coefficient to the exact analytic value is then investigated by progressively increasing the steepness of the approximate step. The convergence at different energy regimes is also investigated.

In the numerical approach, an initial gaussian wavepacket is assumed. The reflection coefficient is thus measured as a function of the ratio of the potential depth to the initial energy of the incoming particle V_0/E and the width parameter a.

The physical system consists of a free particle with energy $E = \frac{p^2}{2m}$, which approaches from the right side ($x > 0$) a potential step of the form:

$$V(x) = \begin{cases} 0 & \text{if } x \geq 0 \\ -V_0 & \text{if } x < 0 \end{cases} \tag{A.1}$$

where $V_0 > 0$.

Since the potential is constant for $x \neq 0$, a plane wave form can be assumed for the incoming, reflected and transmitted waves at positions far from the step compared to the De Broglie wavelength of the particle. Hence by imposing continuity and differentiability conditions at the step, the reflection coefficient, the amplitudes of such waves are obtained.

The reflection coefficient R is defined as the square modulus of the probability density current of the reflected wave to the incoming wave [44], which, in the case of plane waves, reduces to finding the square modulus of the ratio of the two amplitudes. Finally, R can be written in terms of the potential to kinetic energy ratio as [26]:

$$R = \frac{(1 - \sqrt{1 + V_0/E})^2}{(1 + \sqrt{1 + V_0/E})^2} \tag{A.2}$$

A.0.1 Numerical setup

In order to approximate the potential in proximity of the step, a hyperbolic tangent function is used, so that the expression A.1 for the step potential can be approximated in the numerics as:

$$V_N(x; a) = \frac{V_0}{2}[\tanh(x/a) - 1] \tag{A.3}$$

where the decay length a in the hyperbolic tangent function controls the width of the step, so that:

$$\lim_{a \to 0} V_N(x; a) = V(x) \tag{A.4}$$

namely, the function tends to a discontinuous step as a tends to 0. The function $V_N(x; a)$ is shown in Fig.A.1 for $a = 10^{-11}m$.

A particle of mass $m \simeq 5.0 \times 10^{-27}$ kg is considered, which approaches the step at a velocity $v = -2.0$ ms^{-1} (see Herwerth), resulting in a kinetic energy $E = 1.0 \times 10^{-26}$ J. The initial wavepacket is assumed to have an initial mean position value $x_0 = 2.0$ μm and an initial spatial spread of $\sigma_x \simeq 8.0 \times 10^{-8}$ m.
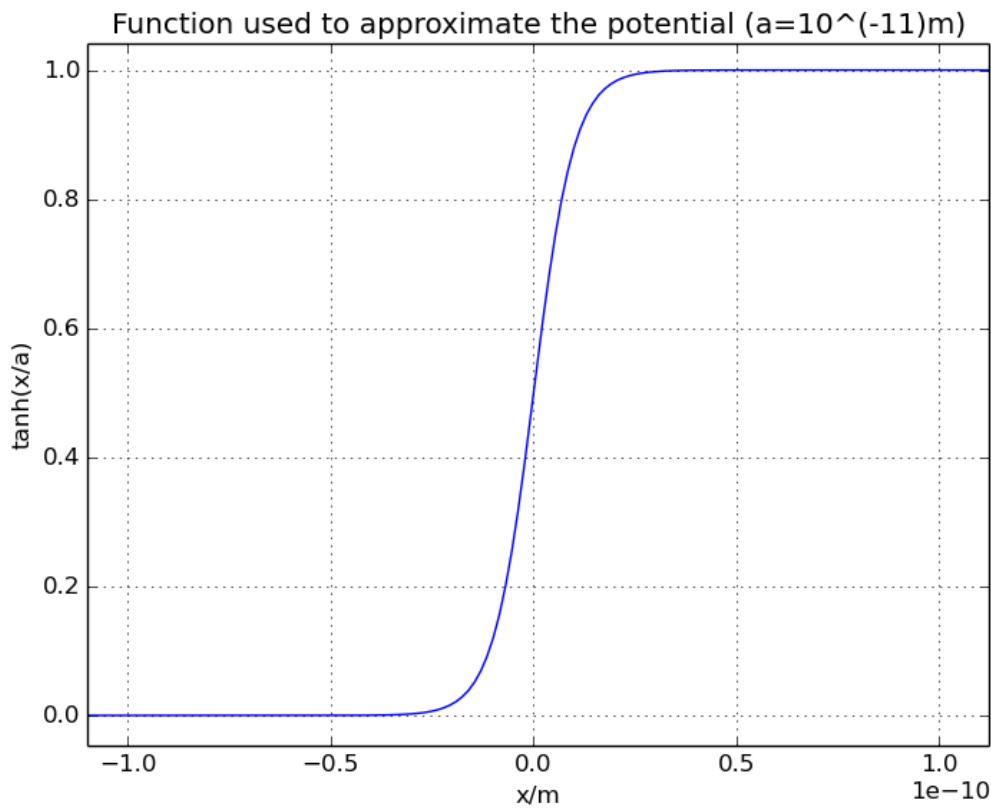
Fig. A.1 The graph shows the function A.3 used to approximate the potential step for $a = 10^{-11}m$.

The position space is sampled from -1.5 μm to 3.0 μm, and the spatial step used varies from $\sim 2.0 \times 10^{-11}$ m to $\sim 1.0 \times 10^{-12}$ m for smaller scaling lengths of the step. Such a dense sampling of the spatial domain is required by the steep behaviour of the potential, which needs to approximate a discontinuity. In fact, a compromise between the steepness of the potential required to effectively approximate the discontinuous potential and the continuity required by numerical scheme needs to be achieved.

The numerical value of the time step is always kept between one and two orders of magnitude larger (in internal units) than the spatial step size, which was found to be a safe choice in order for the numerical procedure to produce sensible results.

A.0.2 Numerical results

Initially, the dependence of R on the potential depth in the numerical and analytic case were compared, as shown in fig.A.2, at a fixed step width parameter $a = 5.0 \times 10^{-10}\ m$.
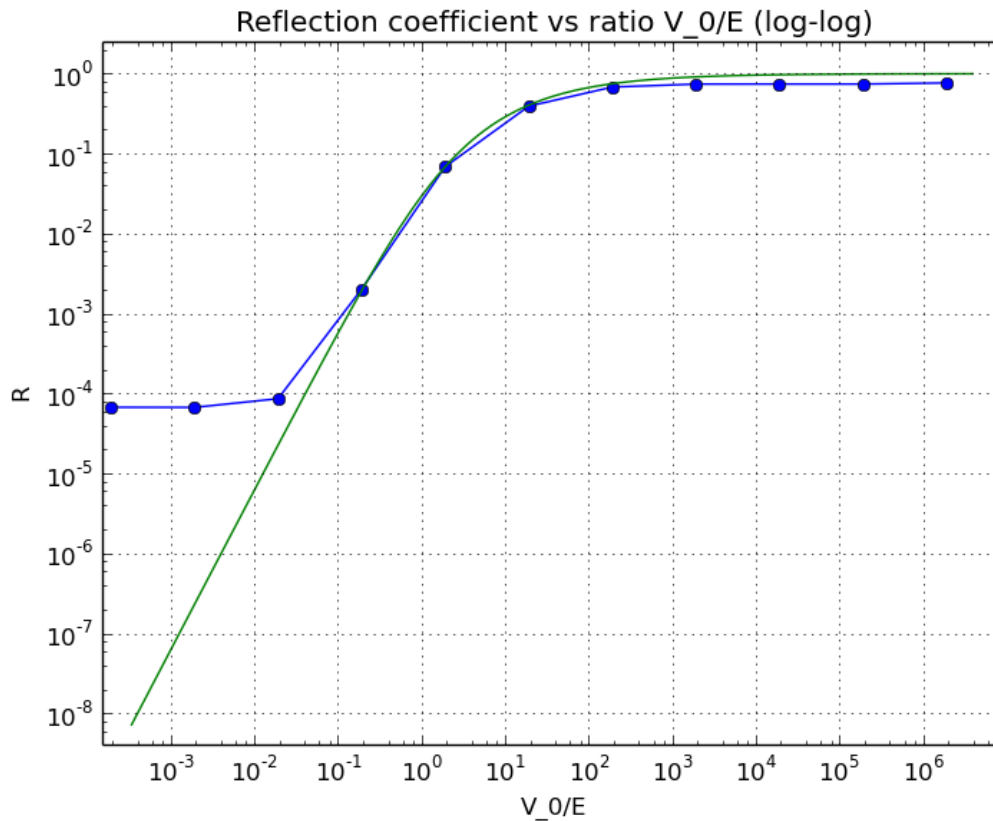
Fig. A.2 The graph shows the results obtained numerically (blue) and analytically (green) for R as a function of the ratio V_0/E. This was performed using a fixed value of the scaling parameter $a = 5 \times 10^{-10}\ m$.

For values of the potential much smaller than the kinetic energy of the particle, R is expected to vanish according to the theory, since the wave is entirely transmitted. However, the evident plateau reached by the curve in Fig.(A.2) suggests that spurious reflection effects affect the measurement of R.

In fact, this effect enabled the finding of artificial reflections which are caused by the numerical filter. These were proved by propagating the wavepacket without a potential and observing the reflections as the transmitted wave is absorbed by the filter. The resulting reflection is shown in Fig.(A.3). This fact has a key importance, in that it hinders the possibility to measure values of QR smaller than such noise. At the present time, our

objectives do not require a higher precision, although the presence of such noise has to be considered in the interpretation of the results. Future studies will be necessary in order to optimise the filter to reduce this effect.
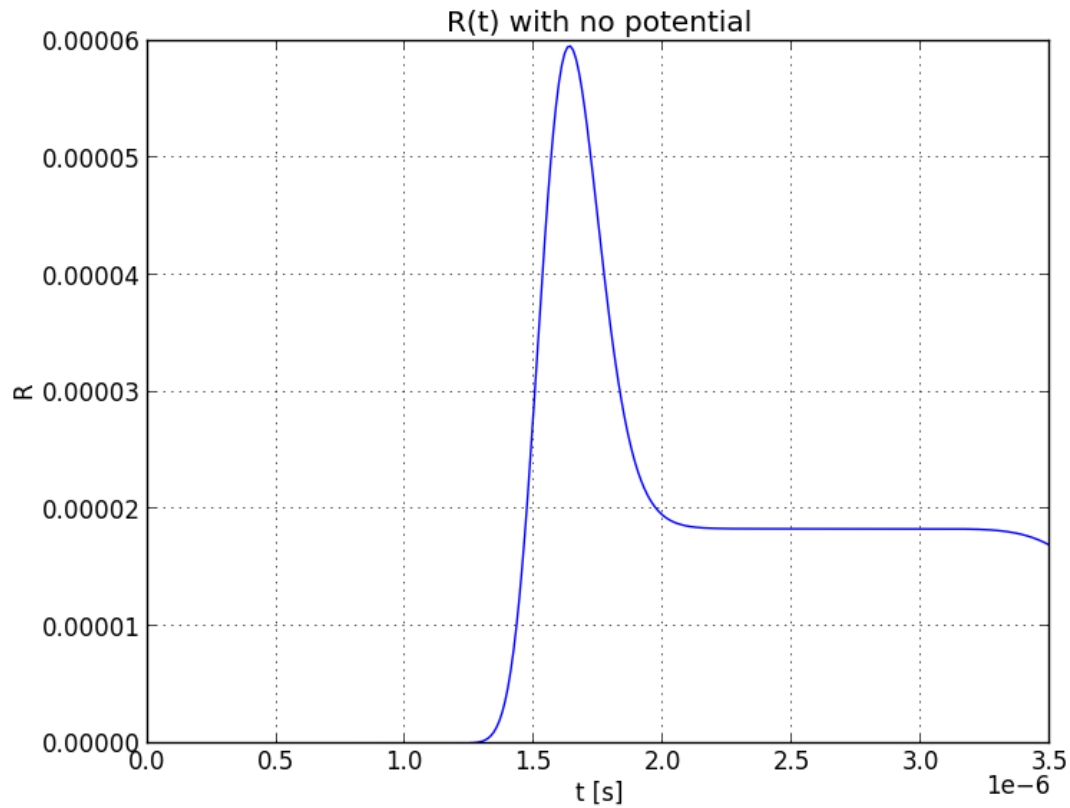
Fig. A.3 The graphs shows the reflection coefficient as a function of time as the wavepacket is propagated in a flat potential. Such unwanted reflection is caused by the filter, as a result of the absorption of the wavefunction towards the negative end of the box being too abrupt. After reaching a peak of 6×10^{-5}, the filter keeps acting on the reflected wavepacket at each timestep, so that R is reduced to 2×10^{-5}, after which the whole wave travels back in the positive x directio, thus yielding a constant value of R.

The results show an overall agreement within a relative error of 10^{-2} in the regime at which the energy of the particle is comparable to the depth of the potential step.

The evident discrepancy for larger values of the ratio V_0/E can be recovered by decreasing the value of the scaling length a as shown below. This clearly requires a denser spatial sampling and a consequently smaller timestep.

A.0.3   Varying the width of the step

In this subsection the behaviour of R as a function of the width parameter a of the step is investigated. Such dependence was studied at two different potential regimes, namely for $V_0/E \simeq 2$ and for $V_0/E \simeq 2 \times 10^2$.

Shallow potential regime

For the shallow potential regime, a ratio $V_0/E \simeq 2$ of potential to kinetic energy was chosen. Fig.A.4 shows the dependence of the numerical results on the width parameter a.

While only minor variations occur for $a < 5 \times 10^{-10}m$, the result for R decreases considerably for $a > 10^{-9}m$. This result is expected, since the shape of the potential does not approximate a step. In fact, as discussed in Sec.(1.2), the steepness of the potential plays a central role in the phenomenon of QR.

On the other hand, it can be clearly seen that the numerical value obtained for R overshoots for values of $a \leq 2.5 \times 10^{-10}m$. The gap between the two values remains then constant. Such overshoot, whose relative size is 10^{-2}, is discussed more in depth at the end of this section.

Deeper potential regime ($V_0/E \simeq 2 \times 10^2$)

The simulations were run at $V_0/E = 192.4$ for different values of a, and the results are shown in shown in Fig.A.5.

The same effect as in the shallow potential case occurs for larger values of the scaling length. Moreover, as the scaling length is decreased, an overshoot is found in this case, although the relative error associated with it in this case is smaller, as shown in Table A.1 . A relative error of 10^{-3} was measured in this case for a step width of $a = 10^{-11}m$.

A.0.4   Discussion and conclusions

The behaviour of the reflection coefficient at different energy regimes, as well as different values of the width parameter of the step was investigated, thus enabling the recognition of an overshoot of the reflectivity as the potential becomes too steep. Such effect resulted in relative errors for the reflectivity of order between 10^{-2} and 10^{-3} in the shallow and deep energy regimes respectively.

In fact, the overshoot was later found (see in particular Sec.1.4) to be a systematic effect caused by the excessive steepness of the potential for a given spatial step size.
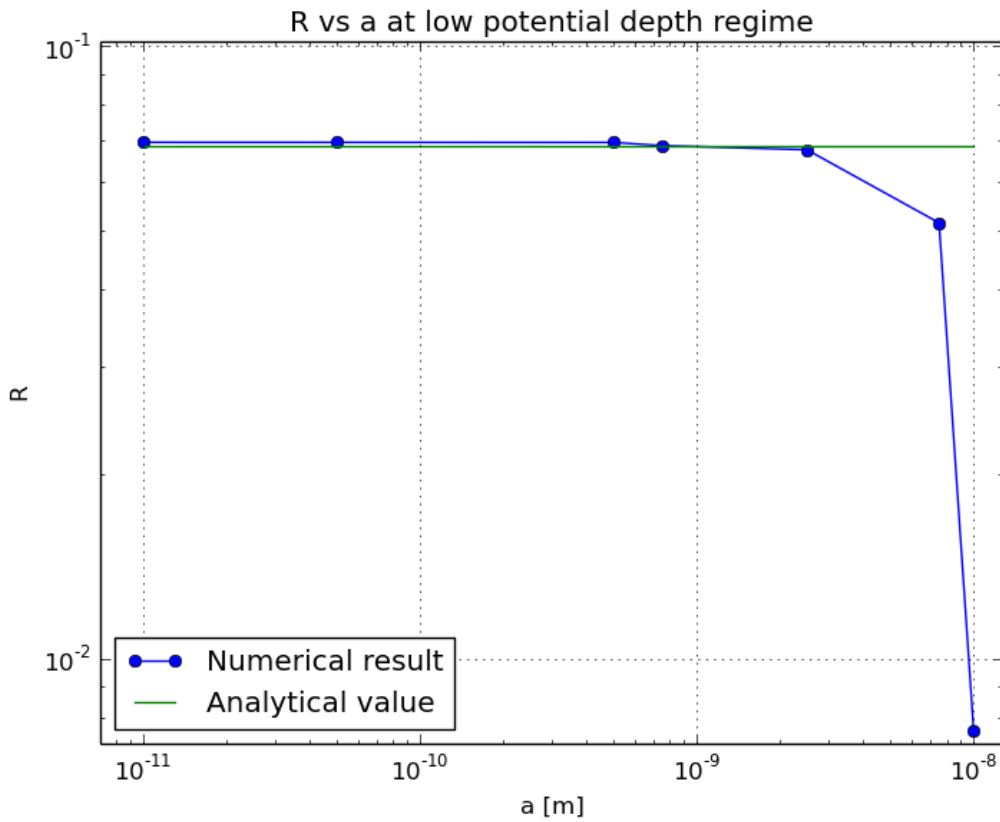
Fig. A.4 Numerical result for the reflection coefficient as a function of the width parameter a of the step. Most values were computed with a numerical grid of 2^{18} grid points. The energy ratio is kept fixed at $V_0/E \simeq 1.924$. The reflection coefficient is comparable to the analytical result for $a < 5 \times 10^{-10}$ before it starts decreasing significantly as the step becomes too smooth.

Furthermore, a systematic error was found as a result of artificial reflections occurring at the filter.

Although further optimisation of the filter will be possible in future studies, this is not among the objectives of the present project. Nevertheless, further thoughts on potential improvements of the numerical filter are given in the final outlook. Overall, this preliminary investigation was successful in the achievement of a better understanding of the influence of the key physical and numerical parameters on the behaviour of R.
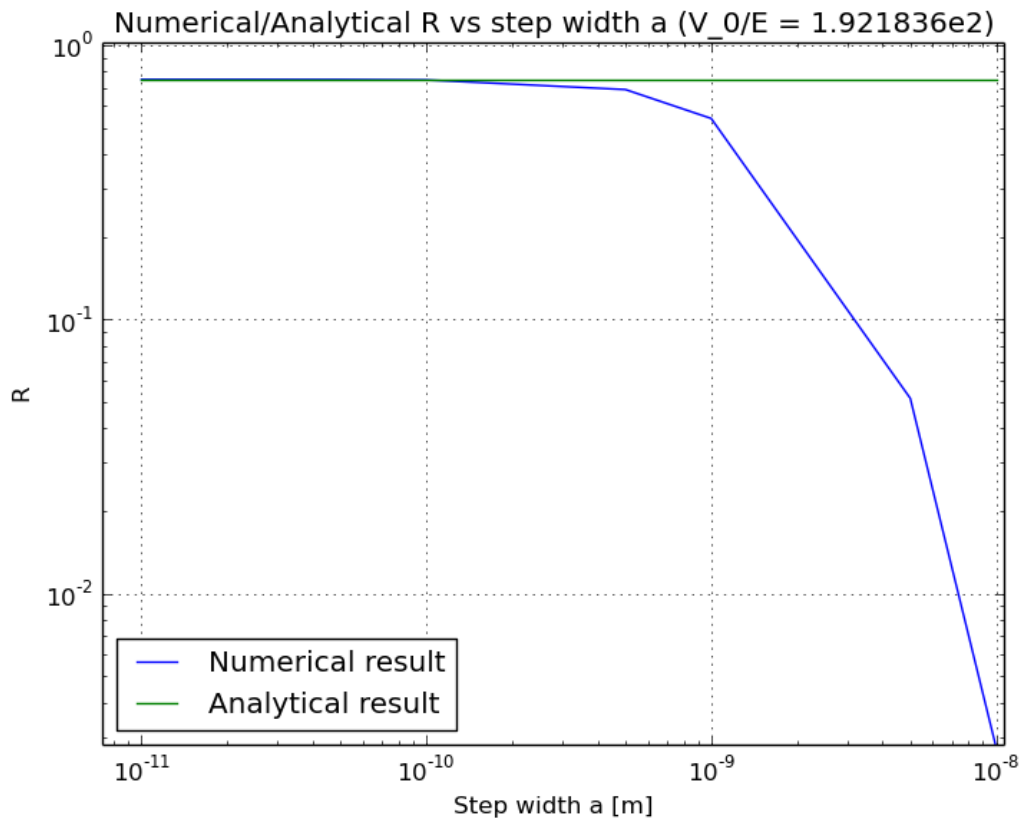
Fig. A.5 Numerical result for the reflection coefficient as a function of the width parameter a of the step for $V_0/E \simeq 2 \times 10^2$.

Step width "a" [m]	R numerical	R analitical
1e-8	0.00276494	0.74954605
5e-9	0.05157853	0.74954605
1e-9	0.54040761	0.74954605
5e-10	0.68870832	0.74954605
1e-10	0.74661044	0.74954605
5e-11	0.74891171	0.74954605
2.5e-11	0.74948996	0.74954605
1e-11	0.74965206	0.74954605

Table A.1 Numerical convergence to the analytical result at different values of the width parameter a.